The Astrophysical Journal Supplement Series, 262:14 (31pp), 2022 September https://doi.org/10.3847/1538-4365/ac7beb

Monitoring AGNs with Hβ Asymmetry. III. Long-term Reverberation Mapping Results of 15 Palomar–Green Quasars

Dong-Wei Bao[1,2], Michael S. Brotherton[3], Pu Du[1], Jacob N. McLane[3], T. E. Zastrocky[3,4], Kianna A. Olson[3], Feng-Na Fang[1,2], Shuo Zhai[1,2], Zheng-Peng Huang[1], Kai Wang[1], Bi-Xuan Zhao[5], Sha-Sha Li[6], Sen Yang[1,2], Yong-Jie Chen[1,2], Jun-Rong Liu[1,2], Zhu-Heng Yao[1,2], Yue-Chang Peng[1,2], Wei-Jian Guo[1,2], Yu-Yang Songsheng[1,2], Yan-Rong Li[1], Bo-Wei Jiang[1,2], David H. Kasper[3], William T. Chick[3], My L. Nguyen[3], Jaya Maithil[3], H. A. Kobulnicky[3], D. A. Dale[3], Derek Hand[3], C. Adelman[3,7], Z. Carter[3,8], A. M. Murphree[3,9], M. Oeur[3,10], S. Schonsberg[3,11], T. Roth[3,12], Hartmut Winkler[13], Paola Marziani[14], Mauro D'Onofrio[15], Chen Hu[1], Ming Xiao[1], Suijian Xue[16], Bożena Czerny[17], Jesús Aceituno[18,19], Luis C. Ho[20,21], Jin-Ming Bai[6], and Jian-Min Wang[1,2,22,23]

(MAHA Collaboration)

[1] Key Laboratory for Particle Astrophysics, Institute of High Energy Physics, Chinese Academy of Sciences, 19B Yuquan Road, Beijing 100049, People's Republic of China; dupu@ihep.ac.cn
[2] School of Astronomy and Space Science, University of Chinese Academy of Sciences, 19A Yuquan Road, Beijing 100049, People's Republic of China
[3] Department of Physics and Astronomy, University of Wyoming, Laramie, WY 82071, USA; mbrother@uwyo.edu
[4] Physics and Astronomy Department, Regis University, Denver, CO 80212, USA
[5] Shanghai Observatory, Chinese Academy of Sciences, 80 Nandan Road, Shanghai 200030, People's Republic of China
[6] Yunnan Observatories, Chinese Academy of Sciences, Kunming 650011, People's Republic of China
[7] Department of Physics & Astronomy, Cal Poly Pomona, Pomona, CA 91768, USA
[8] Department of Physics and Astronomy, Trinity University, San Antonio, TX 78212, USA
[9] Department of Physics, Rhodes College, Memphis, TN 38112, USA
[10] Department of Physics and Astronomy, State Long Beach, Long Beach, CA 90840, USA
[11] Department of Physics and Astronomy, University of Montana, Missoula, MT 59812, USA
[12] Department of Physics & Astronomy, California State University, Sacramento, CA 95747, USA
[13] Department of Physics, University of Johannesburg, P.O. Box 524, 2006 Auckland Park, South Africa
[14] Istituto Nazionale di Astrofisica (INAF), Osservatorio Astronomico di Padova, I-35122 Padova, Italy
[15] Dipartimento di Fisica & Astronomia "Galileo Galilei", Università di Padova, Padova, Italy
[16] Key Laboratory of Optical Astronomy, National Astronomical Observatories, Chinese Academy of Sciences, Beijing 100012, People's Republic of China
[17] Center for Theoretical Physics, Polish Academy of Sciences, Al. Lotnikow 32/46, 02-668 Warsaw, Poland
[18] Centro Astronomico Hispano Alemán, Sierra de los filabres sn, E-04550 Gergal, Almería, Spain
[19] Instituto de Astrofísica de Andalucía (CSIC), Glorieta de la astronomía sn, E-18008 Granada, Spain
[20] Kavli Institute for Astronomy and Astrophysics, Peking University, Beijing 100871, People's Republic of China
[21] Department of Astronomy, School of Physics, Peking University, Beijing 100871, People's Republic of China
[22] National Astronomical Observatories of China, Chinese Academy of Sciences, 20A Datun Road, Beijing 100020, People's Republic of China
Received 2022 March 16; revised 2022 June 7; accepted 2022 June 22; published 2022 August 22

Abstract

In this third paper of the series reporting on the reverberation mapping campaign of active galactic nuclei with asymmetric Hβ emission-line profiles, we present results for 15 Palomar–Green quasars using spectra obtained between the end of 2016–2021 May. This campaign combines long time spans with relatively high cadence. For eight objects, both the time lags obtained from the entire light curves and the measurements from individual observing seasons are provided. Reverberation mapping of nine of our targets has been attempted for the first time, while the results for six others can be compared with previous campaigns. We measure the Hβ time lags over periods of years and estimate their black hole masses. The long duration of the campaign enables us to investigate their broad-line region (BLR) geometry and kinematics for different years by using velocity-resolved lags, which demonstrate signatures of diverse BLR geometry and kinematics. The BLR geometry and kinematics of individual objects are discussed. In this sample, the BLR kinematics of Keplerian/virialized motion and inflow is more common than that of outflow.

Unified Astronomy Thesaurus concepts: Reverberation mapping (2019); Active galactic nuclei (16); Active galaxies (17); Supermassive black holes (1663); Quasars (1319)

Supporting material: machine-readable tables

1. Introduction

The broad emission lines of active galactic nuclei (AGNs), are the primary features in their UV/optical spectra and arise from the photoionization of gas in the broad-line regions (BLRs) by the continuum emission from the accretion disks around the central supermassive black holes (SMBHs). Although the profiles of the broad Balmer emission lines (e.g., Hα, Hβ, Hγ) in AGNs are sometimes well approximated by Gaussian or Lorentzian functions, a fraction of them are more complex and possess

[23] PI of the MAHA Project.

significant asymmetries (redward, blueward, or double-peaked) sometimes with systematic velocity shifts of their peaks (e.g., De Robertis 1985; Sulentic 1989; Marziani et al. 2003a; Eracleous et al. 2012). The physical origin of the profile asymmetries of broad emission lines is far from fully understood, but it is likely that the asymmetries are connected with the kinematics of BLRs or opacity effects.

In past decades, observational studies often focused on emission-line profiles and their correlations with other AGN properties. For example, Boroson & Green (1992) discovered that the Hβ profile tends to be red asymmetric if the Fe II emissions are weak and the [O III] lines are strong (the main variations in the so-called Eigenvector 1). Marziani et al. (2003b) divided a sample of AGNs into several bins with different black hole (BH) masses and Eddington ratios and investigated the systematic properties of the median profiles of broad Hβ in each bin, showing that redward asymmetries are observed at a low Eddington ratio. Netzer & Trakhtenbrot (2007) studied AGNs from the Sloan Digital Sky Survey (SDSS) and found that the fractional flux of the red part of the Hβ line shows a positive correlation with luminosity and a negative correlation with the flux ratio of Fe II/Hβ. Hu et al. (2008) discovered that the Hβ line shows a more significantly red asymmetry if the Fe II emission lines have stronger redshifted velocities.

Additionally, theoretical efforts were made to understand the diversity of emission-line profiles. Capriotti et al. (1979) proposed that the line asymmetries could be attributed to optically thick inflowing or outflowing BLR clouds. Ferland et al. (1979) calculated asymmetric profiles from an expanding BLR by taking into account Balmer self-absorption of optically thick clouds. Chen et al. (1989) and Chen & Halpern (1989) found that a relativistic Keplerian disk can explain the observed asymmetric and double-peaked profile observed in Arp 102B. Eracleous et al. (1995) suggested that a relativistic eccentric disk could account for observed asymmetries. Storchi-Bergmann et al. (2003) used the spiral arms in a disk to explain the Hα line profile variations of NGC 1097. Wang et al. (2017) suggested that the BLR could be formed through tidal disruption of clumps from a dusty torus, showing asymmetric profiles due to the infall of the captured gas. Asymmetries of profiles generated by this model are generally consistent with profiles of Palomar–Green (PG) quasars. Furthermore, supermassive binary black holes (SMBBHs) were also recently proposed to explain double-peaked profiles (e.g., Shen & Loeb 2010; Bon et al. 2012; Li et al. 2016; Ji et al. 2021).

The reverberation mapping (RM) technique (Blandford & McKee 1982; Peterson 1993) is a powerful tool for investigating the geometry and kinematics of BLRs, by monitoring the delayed response of the broad emission lines with respect to the continuum variation, and has been carried out for more than a hundred AGNs over the past several decades. Before 2000, investigations focused on, for example, bright but heterogeneous samples of Seyfert 1 galaxies (Peterson et al. 1998), PG quasars (Kaspi et al. 2000), or intensive studies of some individual objects (e.g., International AGN Watch project; see Clavel et al. 1991; Peterson et al. 2002). These efforts established a general understanding of the RM properties of AGNs. Since 2000, significant progress has been made by dedicated RM projects with different goals. For example, the Lick AGN Monitoring Project (LAMP; see, e.g., Bentz et al. 2008; Barth et al. 2015; U et al. 2022) resolved the BLR kinematics of some local Seyfert galaxies. The super-Eddington accreting massive black holes (SEAMBHs) project (e.g., Du et al. 2014, 2015, 2016b, 2018b) focuses on the AGNs with the highest accretion rates and found shortened time lags compared to other objects of similar luminosity. Industrial-scale RM campaigns like the SDSS RM project (e.g., Shen et al. 2016; Grier et al. 2017), and the Australian Dark Energy Survey (OzDES) RM program (Yu et al. 2021) use fiber-fed instruments and can obtain the time delays of multiple objects in the field of view simultaneously. Barth et al. (2013) and Hu et al. (2015) measured the time lags of Fe II lines. Rafter et al. (2011) and Woo et al. (2019) monitored intermediate-mass black holes, while Rakshit et al. (2019) and Li et al. (2021) observed luminous nearby quasars (e.g., 5100 Å luminosity $\gtrsim 10^{45}$ erg s^{-1}). Some long-term projects aim to measure C IV or C III] emission lines in high-redshift quasars in a time span of decades (Kaspi et al. 2017, 2021; Lira et al. 2018). There are also many recent campaigns for small samples of (or individual) interesting AGNs (e.g., Denney et al. 2009; Grier et al. 2012; Lu et al. 2016; Fausnaugh et al. 2017; De Rosa et al. 2018; Zhang et al. 2018; Czerny et al. 2019; Hu et al. 2020b; Zajaček et al. 2020, 2021; Oknyansky et al. 2021).

To understand the kinematics associated with the asymmetries of emission-line profiles and to explore the evolution of BLR gas, we initiated a dedicated RM campaign in 2016 named the Monitoring AGNs with Hβ Asymmetry (MAHA) project. We focus on AGNs with asymmetric (or double-peaked) emission lines, which are more likely connected with complicated BLR geometry or kinematics. Another goal of the MAHA project is to search for SMBBH candidates from transfer functions (also called "velocity-delay maps") produced by RM (Wang et al. 2018; Kovačević et al. 2020; Songsheng et al. 2020).

We have previously published the RM results of seven Seyfert galaxies observed from the end of 2016–2017 May (Du et al. 2018a; hereafter Paper I and Brotherton et al. 2020; hereafter Paper II). Some of the objects show very complicated signatures in their velocity-resolved lags (e.g., Ark 120 and Mrk 6) or velocity-delay maps (e.g., Mrk 79), which are difficult to interpret as simple inflow, outflow, or virialized motions (see Papers I and II). The discovery of the diverse BLR kinematics in Seyfert galaxies with asymmetric line profiles (Papers I and II) motivates us to consider whether the BLR geometry and kinematics are also complex in more luminous quasars with asymmetric Hβ.

The PG sample of objects with ultraviolet excesses (Schmidt & Green 1983; Boroson & Green 1992) includes subsamples of quasars that have been extensively studied in almost all wavelengths of the electromagnetic spectrum and some have already been spectroscopically monitored for RM (e.g., Kaspi et al. 2000; Bentz et al. 2009; Grier et al. 2012; Barth et al. 2015; Zhang et al. 2018; Hu et al. 2020a, 2020b). The asymmetries of their emission-line profiles have been investigated using single-epoch spectra (Boroson & Green 1992; Marziani et al. 2003b), but not systematically in the time domain. It is valuable to investigate the geometry and kinematics of their BLRs for the PG quasars with significantly asymmetric emission lines by the velocity-resolved lags (e.g., Bentz et al. 2009; Denney et al. 2010; Du et al. 2016a) or velocity-delay maps (e.g., Grier et al. 2013; Xiao et al. 2018; Horne et al. 2021). As the third paper of the MAHA series, we

Table 1
Basic Information of the 15 PG Targets

Name	Other Names	R.A.	Decl.	z	A	A (Boroson+92)	Observatories	Previous RM
PG 0007+106	Mrk 1501, III Zw 2	00:10:31.0	+10:58:29	0.0872	−0.022	−0.046	WIRO, Asiago, SAAO	(1)
PG 0049+171	Mrk 1148	00:51:54.7	+17:25:59	0.0645	−0.063	−0.047	WIRO	
PG 0923+129	Mrk 705, Ark 202	09:26:03.3	+12:44:03	0.0288	−0.072	−0.031	WIRO	
PG 0947+396		09:50:48.4	+39:26:51	0.2055	−0.116	−0.148	WIRO	
PG 1001+054		10:04:20.1	+05:13:00	0.1601	+0.065	+0.082	Lijiang	
PG 1048+342		10:51:43.8	+33:59:27	0.1671	−0.226	+0.045	WIRO	(2)*
PG 1100+772	3C 249.1	11:04:13.6	+76:58:58	0.3115	−0.106	−0.097	WIRO & Asiago	
PG 1202+281	GQ Com	12:04:42.1	+27:54:12	0.1650	−0.095	−0.298	WIRO & Asiago	
PG 1211+143		12:14:17.6	+14:03:13	0.0809	+0.039	−0.003	Lijiang & CAHA	(2)
PG 1310−108		13:13:05.7	−11:07:42	0.0343	−0.112	−0.075	WIRO	
PG 1351+640		13:53:15.8	+63:45:46	0.0882	−0.139	+0.136	WIRO	(2)*
PG 1351+695	Mrk 279	13:53:03.4	+69:18:29	0.0305	−0.043		WIRO	(3,4,5)
PG 1501+106	Mrk 841	15:04:01.2	+10:26:16	0.0364	−0.071	−0.039	WIRO, Asiago, SAAO	(6)
PG 1534+580	Mrk 290	15:35:52.3	+57:54:09	0.0302	−0.109	+0.044	WIRO	(7)
PG 1613+658	Mrk 876	16:13:57.1	+65:43:10	0.1211	−0.183	−0.207	WIRO	(2,8)

Note. A is a dimensionless parameter to describe the asymmetry, which is measured from our campaign (see Section 2.1). A (Boroson+92) is the asymmetry parameter listed in Boroson & Green (1992). References: (1) Grier et al. (2012), (2) Kaspi et al. (2000), (3) Maoz et al. (1990), (4) Santos-Lleó et al. (2001), (5) Barth et al. (2015), (6) Brotherton et al. (2020), (7) Denney et al. (2010), (8) Minezaki et al. (2019). * means that the previous RM campaign did not successfully measure the time lag of Hβ.

(This table is available in machine-readable form.)

report here the RM observations of 15 PG quasars, most with significantly asymmetric Hβ emission lines.

The paper is organized as follows. The target selection and the observations are given in Section 2. The analyses are provided in Section 3, including the mean and rms spectra, the light curves, the line widths, the time-lag measurements, the black hole masses, and the velocity-resolved time lags. The discussion of individual objects is in Section 4. Finally, in Section 5, we briefly summarize the present paper.

2. Observations

2.1. Targets

The primary goal of the MAHA project is to monitor the AGNs showing current or historical asymmetric emission-line profiles in order to investigate the BLR geometry and kinematics, their evolution, and the possible presence of SMBBHs. Boroson & Green (1992) adopted the line asymmetry parameter

$$A = \frac{[\lambda_c(3/4) - \lambda_c(1/4)]}{\Delta\lambda(1/2)}, \quad (1)$$

defined by De Robertis (1985), and measured the asymmetries of the Hβ emission lines in PG quasars, where $\lambda_c(3/4)$ and $\lambda_c(1/4)$ are the central wavelengths where the profiles are $3/4$ and $1/4$ of the peak value, respectively, and $\Delta\lambda(1/2)$ is the FWHM of emission line. $A < 0$ indicates that the emission line has a profile with a more pronounced red wing, while $A > 0$ means the line has a stronger blue wing (see Figure 1 in Paper I). Boroson & Green (1992) demonstrated that the A parameter is positively correlated with the relative strength of Fe II with respect to Hβ in PG quasars and some of them have strong asymmetries with $A \lesssim -0.1$ or $A \gtrsim 0.1$. Based on the asymmetry measurements of Boroson & Green (1992), we selected five PG quasars (PG 0947+396, PG 1100+772, PG 1202+281, PG 1310−108, and PG 1613+658) with significant red asymmetries ($A \approx -0.08$ to -0.3) and four PG quasars (PG 1001+054, PG 1048+342, PG 1351+640, and PG 1534+580) with moderate-to-significant blue asymmetries ($A \approx 0.05$–0.15) as our MAHA targets from the PG sample in Boroson & Green (1992). It is intriguing that the Hβ profile of PG 1048+342 has changed to red asymmetry in our observations (see its A parameter measurements from our campaign in Table 1).

We also selected an additional six PG quasars as RM targets: PG 0007+106, PG 0049+171, PG 0923+129, PG 1211+143, PG 1351+695, and PG 1501+106. The radio-emission variability of PG 0007+106 demonstrates quasiperiodicity/periodicity (with a period of ∼5 yr; see Teräsranta et al. 2005; Li et al. 2010), which is potentially caused by jet precession. SMBBHs are a possible cause of jet precession (Begelman et al. 1980; Romero et al. 2000); thus we chose this object as our target. The line profile of PG 1211+143 was almost symmetric in Boroson & Green (1992) but showed mild blue asymmetry recently (see Table 1). PG 1351+695 displayed significant blue asymmetry in 2011 (Barth et al. 2015; Williams et al. 2018). PG 1501+106 showed weak red asymmetry in Boroson & Green (1992); however, this asymmetry became stronger in 2017–2020 (see Table 1). The Hβ emission-line profiles of PG 0049+171 and PG 0923+129 were only weakly asymmetric (Boroson & Green 1992), but we included them in our target list as they fit well into our program schedule (showing stronger red asymmetry in our campaign). Table 1 provides for each target the coordinates, redshifts, asymmetries measured in our campaign (from an individual exposure with a high signal-to-noise (S/N) ratio) and from Boroson & Green (1992), and the specific telescopes used. The mean spectra of our targets are displayed in Figure 1.

2.2. Spectroscopy

The spectroscopic observations were carried out using the 2.3 m telescope of the Wyoming Infrared Observatory (WIRO) in the United States, the Lijiang 2.4 m telescope of the Yunnan Observatories of the Chinese Academy of Sciences in China,

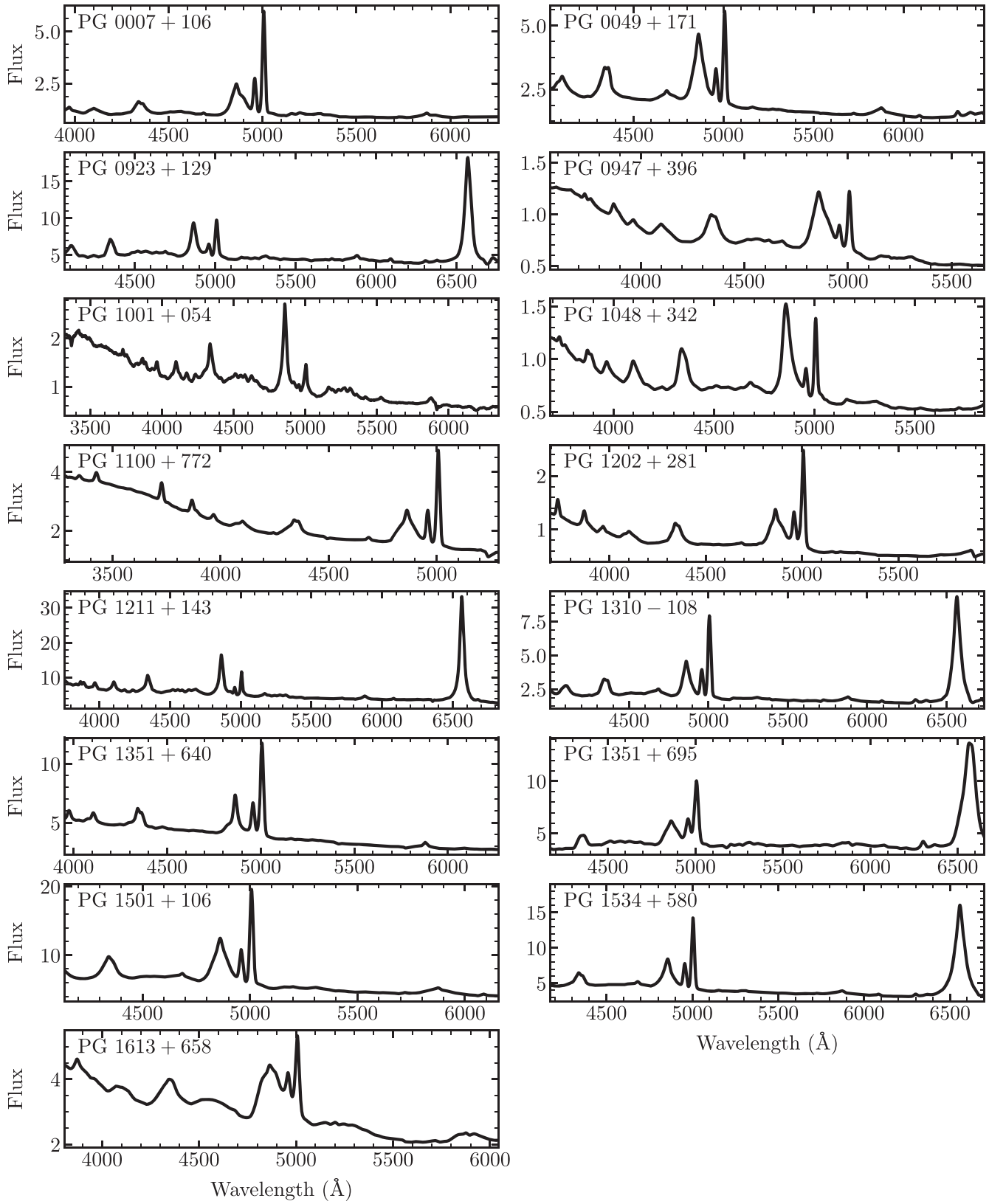

Figure 1. Mean spectra (observed flux density versus rest-frame wavelength) of the objects. Flux units are 10^{-15} erg s^{-1} cm^{-2} Å^{-1}.

the 2.2 m telescope of the Calar Alto Astronomical Observatory of Centro Astronómico Hispano-Alemán (CAHA) in Spain, the Copernico 1.82 m telescope of the Italian National Institute for Astrophysics (INAF) at Mount Ekar in Italy, and the Sutherland 1.9 m telescope at the South African Astronomical Observatory (SAAO) in South Africa. The sites at which individual objects were observed are listed in Table 1. Observations for some objects date back to 2016 December and continued until the northern spring of 2021 for all targets except PG 1211+143 (for which observations concluded in

2017 July). We monitored most of the objects for more than one year. To investigate the potential changes of the BLRs in different years, we usually divided the data for each target into observing seasons bounded by the periods when objects were inaccessible. We did not divide the observations of PG 1100 +772, PG 1351+640, PG 1351+695, PG 1534+580 into segments because the seasonal gaps were small or their variation timescales are too long to get reliable lag measurements from individual seasons (see figures in the following sections). We divided the data of PG 1613+658 into only two seasons because of its relatively long variation timescale. Our observations of PG 0923+129, PG 1211+143, and PG 1310 −108 span only one season. The detailed beginning and end dates, spectroscopic epochs, and cadences for different seasons are listed in Table 3. The spectra obtained from the five telescopes were all reduced using standard procedures (including the corrections of bias and flat field and the wavelength calibration) using IRAF v2.16. Here we briefly introduce the settings of the instruments, apertures, and calibration of the observations at these telescopes.

2.2.1. WIRO Data

We performed RM at WIRO using a 900 l mm^{-1} grating, which provides a dispersion of 1.49 Å $pixel^{-1}$ and a wavelength range of ∼4000–7000 Å. To minimize slit losses and their influence on the flux calibration, a 5″ wide slit oriented north–south was adopted (wider than the typical seeing of ~2″–3″). Spectrophotometric standard stars (usually BD+28°4211, G191B2B, Feige 34, and Hz 44) were used for flux calibration. We used an extraction aperture from −6.″84 to 6.″84, with background windows [−15.″2, −7.″6] and [7.″6, 15.″2] relative to the object's nuclear position. We adopted the [O III]-based technique (e.g., van Groningen & Wanders 1992; Fausnaugh 2017) to perform the relative flux calibration. Where necessary, the spectra of the targets are artificially broadened to achieve the same spectral resolution throughout and then scaled according to their [O III] fluxes (see more details in Paper I). The fiducial [O III] fluxes were determined using the spectra taken in photometric conditions. The [O III] λ4959 lines of PG 1202+281, PG 1351+640, and PG 1351 +695 overlap with their [O III]λ5007 because of their broad line widths (please note that, during the [O III]-based flux calibration, the original spectra were broadened). We used both of the [O III] lines to do the flux calibration in these cases.

During each night, we took three to four consecutive exposures in order to both improve the S/N ratios and evaluate the calibration accuracy by checking their differences. The spectra taken during the same night (after the [O III] calibration) were combined to produce the spectrum for that epoch. In addition to Poisson noise, the difference between the consecutive exposures during the night is caused by the varying weather conditions, seeing variations, or tracking variations during the exposures. This systematic uncertainty was estimated by comparing the fluxes of the exposures in a wide range of wavelengths (4740–5125 Å, effectively eliminating the contribution from Poisson noise) and was added to the error of the continuum and emission-line fluxes of the corresponding epoch using quadratic summation (see more details in Paper I).

Table 2
R.A. and Decl. of the Comparison Stars for Spectroscopy of Two Lijiang Targets

Target	$R.A._{comp}$	$Decl._{comp}$
PG 1001+054	10:04:24	+05:15:29
PG 1211+143	12:13:59	+14:05:16

2.2.2. Lijiang Data

We used the Yunnan Faint Object Spectrograph and Camera (YFOSC) installed in the Lijiang 2.4 m telescope, which is an instrument both for low-resolution spectroscopy and imaging. Grism 14 (with a resolution of 1.8 Å $pixel^{-1}$ and a wavelength range of 3800–7200 Å) and a 2.″5-wide slit were adopted in the campaign. The spectra were extracted in an aperture of ±4.″25 around the nuclear position, with background windows [−14.″15, −7.″36] and [7.″36, 14.″15]. The field de-rotator of the telescope makes it easy to rotate the slit accurately; thus we perform the flux calibration by placing a comparison star simultaneously in the slit (Maoz et al. 1990; Kaspi et al. 2000; see more details in Du et al. 2014). The advantage of the comparison-star-based calibration technique is that it can accurately correct for the changes of the wavelength-dependent atmosphere extinction in different nights. The information of the comparison stars are listed in Table 2. The fiducial spectra of the comparison stars were generated from the data in good weather conditions (calibrated by the spectrophotometric standard stars Feige 34 and Hiltner 600). The target spectra were flux-corrected by scaling the comparison stars to standard values. In order to ensure that the comparison stars were not variable during observations, we performed differential photometry using several field stars. The standard deviations of the photometric light curves of the comparison stars are ∼1% and much smaller than the variation amplitudes of the targets, which means that they can be treated as calibration standards. Similar to the WIRO observations, we took two to three consecutive exposures each epoch. We combined them to obtain the individual-night spectra. In addition, we corrected the small wavelength-calibration uncertainties of the spectra according to their [O III] emission lines before producing the light curves.

2.2.3. CAHA Data

Several spectra of PG 1211+143 were taken using the CAHA 2.2 m telescope from 2017 May to August using the Calar Alto Faint Object Spectrograph (CAFOS). We took the spectra using Grism G-200 and a 3.″0-wide long slit. The wavelength coverage is from 4000 to 8000 Å (with a dispersion of 4.47 Å $pixel^{-1}$). The spectra were extracted in an aperture of ±5.″58, with background windows [−23.″85, −6.″30] and [6.″30, 23.″85]. Similar to the observations at Lijiang, we also adopted the comparison-star-based calibration technique. The coordinates of the comparison star are listed in Table 2. The calibration procedures are the same as for the Lijiang data (see Section 2.2.2).

2.2.4. Asiago Data

For PG 0007+106, PG 1100+772, PG 1202+281, and PG 1501+106, some of the data points come from the Asiago 1.82 m telescope. The spectra were taken using the Asiago Faint Object Spectrograph and Camera (AFOSC), which is a focal reducer instrument similar to YFOSC and CAFOS, with a 4.″2 slit. For PG 0007+106 and PG 1501+106, Grism VPH7

was used, with a wavelength coverage of 3200–7000 Å and a dispersion of 2.95 Å pixel^{-1}. For PG 1100+772 and PG 1202+281, Grism VPH6 was used, with a wavelength coverage of 4500 to 10,000 Å with a dispersion of 2.95 Å pixel^{-1}. We also adopted the [O III]-based calibration, similar to that in the WIRO data reduction. We extracted the spectra using a window of ± 30 pixels (corresponding to ±7.″8). The background was determined using the windows [−13″, −6.″76] and [6.″76, 13″] on both sides of the objects.

2.2.5. SAAO Data

We also took spectra using the SAAO 1.9 m telescope for PG 0007+106 and PG 1501+106. The 600 lines mm^{-1} grating and a slit width of 4.″04 were used. The flux calibration was also performed using the [O III]-based technique. More details of the observations and data reduction can be found in Winkler & Paul (2017). We extracted the spectra using a window of ±6 pixels (corresponding to ±8.″16). The background was determined using the windows [−20.″4, −10.″9] and [10.″9, 20.″4] on both sides of the objects.

2.3. Photometry

The YFOSC and CAFOS instruments can also perform imaging observations. For PG 1001+054 and PG 1211+143, we took Johnson *V*-band images and carried out differential photometry for the targets and the in-slit comparison stars using several other stars in the same fields. The purpose was (1) to make sure that the in-slit comparison stars were not variable during our campaign and (2) to check the flux calibration accuracy of the spectroscopic observations. The fluxes of the targets and comparison stars were extracted using circular apertures with radii of 5.″66 and 5.″30 for YFOSC and CAFOS, respectively. The typical exposure times were 20–50 s. For PG 1001+054, the small scatter of the photometric light curve of the comparison star is at the level of ∼1%–2%, which is stable enough for calibrations. While the comparison star of PG 1211+143 is not in the field of view for photometry, the consistency between its photometric and spectroscopic continuum light curves indicates that its comparison star did not vary significantly and our calibration procedures appear accurate.

To improve the cadence and extend the temporal coverage of the continuum light curves, we also employ archival time-domain photometric data from the All-Sky Automated Survey for SuperNovae[24] (ASAS-SN) and the Zwicky Transient Facility[25] (ZTF). The ASAS-SN project (Shappee et al. 2014; Kochanek et al. 2017) started in 2013 to identify transients and variable sources. Objects with magnitudes between 8 mag and 17 mag in the whole sky are monitored. The details of the data reduction are provided in Shappee et al. (2014) and Kochanek et al. (2017). ZTF makes use of the Palomar 48 inch Schmidt telescope and provides high-quality photometric light curves for objects with magnitudes $\lesssim 20$ (Masci et al. 2019). As of 2021 May, there were six data releases in ZTF. We employ the light curves from ASAS-SN (*g* and *V* bands) and ZTF (*g* and *r* bands) to supplement our photometric and spectroscopic continuum light curves. Considering that the scatter in the ASAS-SN light curves is larger than that of our spectroscopic continuum and the ZTF light curves, we adopted the ASAS-SN data only if they can significantly lengthen the continuum light curves or supplement their temporal coverage (PG 0049+171, PG 0923+129, PG 1211+143, PG 1351+695, PG 1501+106, PG 1534+580, and PG 1613+658). Otherwise, the ZTF light curves are used in the present work.

[24] http://www.astronomy.ohio-state.edu/asassn/index.shtml
[25] https://www.ztf.caltech.edu/

3. Analysis

3.1. Mean and rms Spectra

To check the general Hβ profiles, evaluate their variation amplitudes, and investigate their changes in different seasons, we calculated the mean and rms spectra of the objects for the whole campaign as well as for individual seasons (see Figures 2–16) using

$$\bar{F}_\lambda = \frac{1}{N}\sum_{i=1}^{N} F_\lambda^i, \tag{2}$$

and

$$S_\lambda = \left[\frac{1}{N}\sum_{i=1}^{N}(F_\lambda^i - \bar{F}_\lambda)^2\right]^{1/2}, \tag{3}$$

respectively. Here F_λ^i is the *i*th spectrum of the object, and *N* is the number of its spectra. The narrow [O III] emission lines in the rms spectra are extremely weak or negligible compared to the mean spectra of the same objects, which indicates that our calibration procedure works well. Only the [O III] lines in the rms spectrum of PG 1211+143 have some residual signals. This is caused by the variation of spectral resolution in its exposures with different seeing rather than the flux variations of the [O III] lines. We took the spectra at Lijiang/CAHA (see Table 1) and performed the flux calibration based on the comparison star (see Section 2.2.2) for this object. The variable spectral resolution was not corrected. We measure the standard deviation of [O III]λ5007 flux to be ∼3%, which indicates the reliability of our calibration procedures.

The rms spectra of several objects in some seasons only show weak Hβ emission lines or even what appear to be "absorption lines." There are two main reasons for this: (1) the variation amplitudes of the Hβ fluxes in the corresponding periods are significantly smaller than those in other seasons (e.g., Season 4 in PG 0947+396; Season 2 in PG 1202+281 and PG 1501+106; see Figures 5, 9, and 14), and (2) the variations of their Hβ light curves show reverse modulation with respect to the continuum light curves–in other words, the peaks (troughs) of the Hβ fluxes happen to appear during the troughs (peaks) of the continuum fluxes (see, e.g., the light curves of PG 0947+396 in Season 2 and PG 1202+281 in Seasons 1 and 3; in Figures 5 and 9). To check if the contribution from the reverse variations of the continuum can really weaken the emission-line signals in the rms spectra, we subtracted the continuum beneath the Hβ lines, determined from the linear interpolation between two continuum windows on both sides, from each individual spectrum before calculating the rms spectra for those objects in which the rms spectra showed very weak or "absorption-like" Hβ signals. The continuum-cleaned rms spectra of PG 0049+171, PG 0947+396, PG 1202+281, PG 1351+640, and PG 1501+106 are plotted in Figures 3, 5, 9, 12, and 14, respectively. The continuum-cleaned rms spectra have much stronger Hβ emission lines than the original rms spectra, consistent with

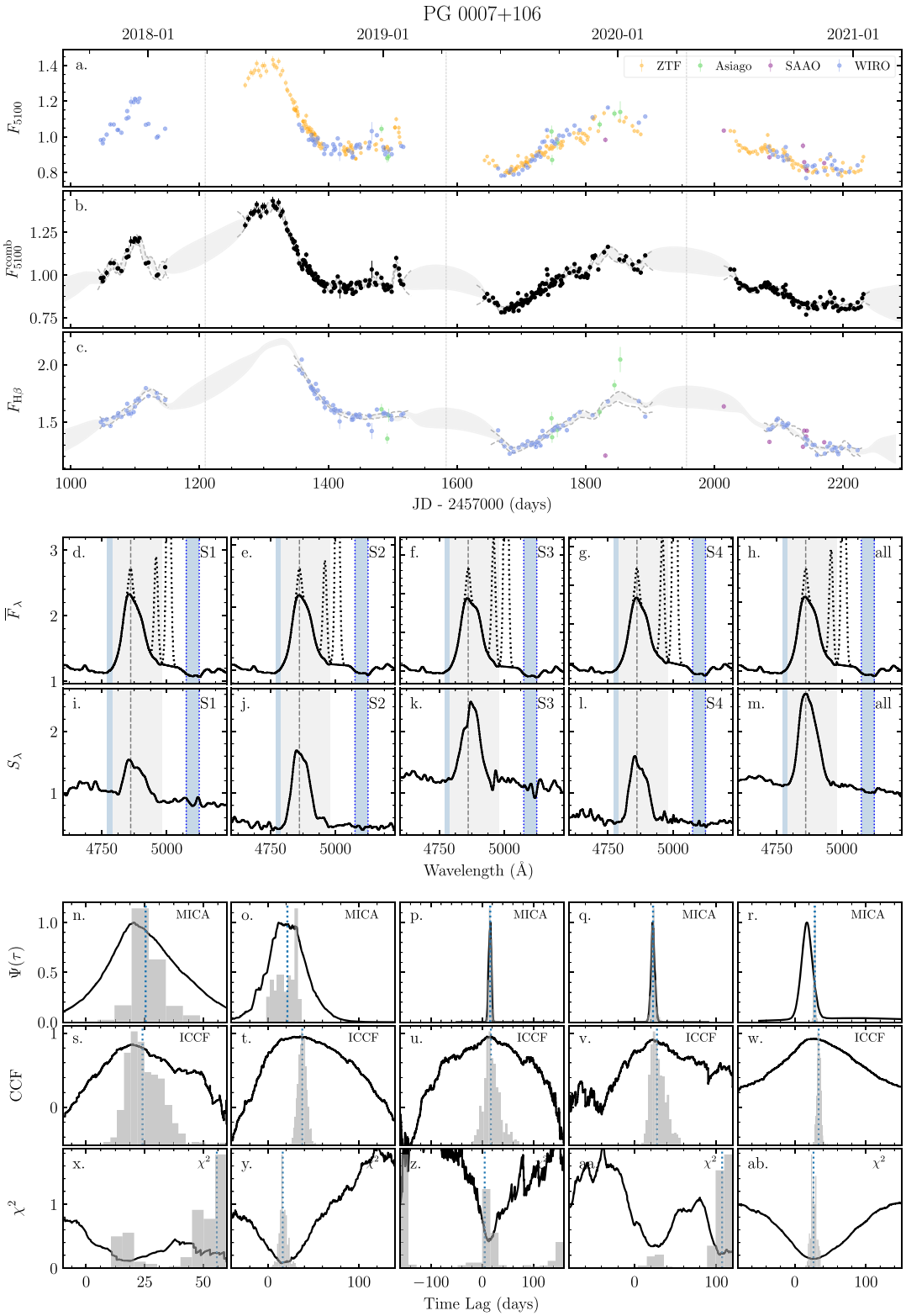

Figure 2. Time-series analysis of PG 0007+106. Panels (a), (b), and (c) are the scaled continuum, combined continuum, and Hβ light curves. The units are 10^{-15} erg s^{-1} cm^{-2} Å^{-1} for panels (a) and (b) and 10^{-13} erg s^{-1} cm^{-2} for panel (c). The gray dotted lines separate different seasons. The gray shadow and gray dashed lines are the MICA reconstructions for the whole light curve and single seasons, respectively. Panels (d)–(m) are the mean (rms) spectra of the seasons and the entire light curve in the rest frames. The black dashed lines are the narrow-line-subtracted mean spectra. The gray and blue shades mark the integration and background windows for Hβ fluxes, and the two blue dotted lines mark the 5100 Å continuum window. The units in panels (d)–(m) are 10^{-15} erg s^{-1} cm^{-2} Å^{-1} (10^{-16} erg s^{-1} cm^{-2} Å^{-1}). Panels (n)–(ab) are the MICA, ICCF, and χ^2 results for the corresponding seasons and the entire light curve (in observed frame). The gray histograms are the distributions of the centroid lags obtained from MICA (CCCDs from ICCF or lag distributions from χ^2 method) in panels (n)–(r), (s)–(w), or (x)–(ab). The blue dotted lines are the median of the distributions. The error bars shown in the light curves do not include the systematic uncertainties in Table 4 (they are used in the time-series analysis in Section 3.5; see also Section 3.2).

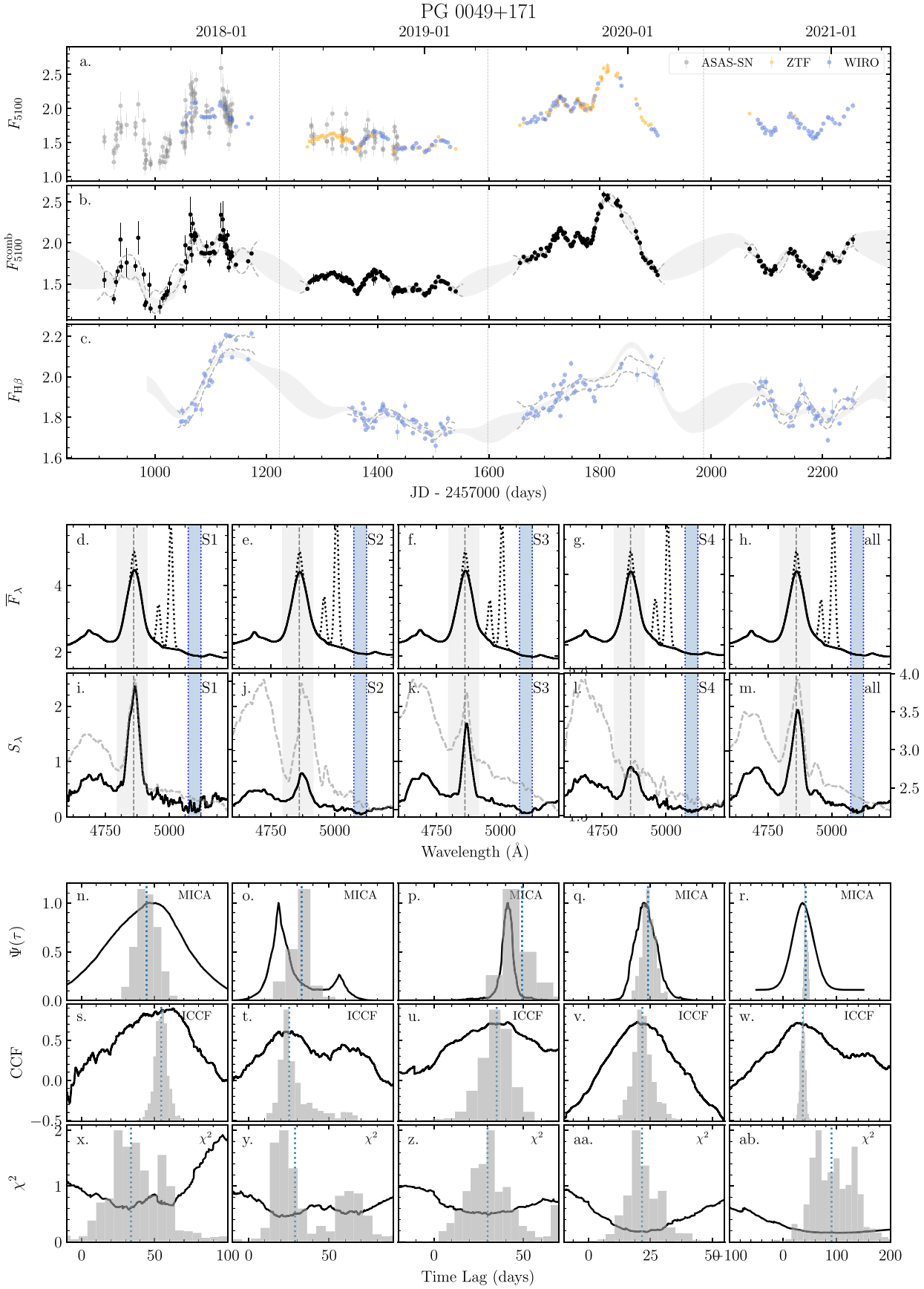

Figure 3. Time-series analysis of PG 0049+171. The gray and black dashed lines in panels (i)–(m) are the original and continuum-cleaned rms spectra (see more details in Section 3.1). The meanings of the other panels, lines, and histograms are the same as in Figure 2.

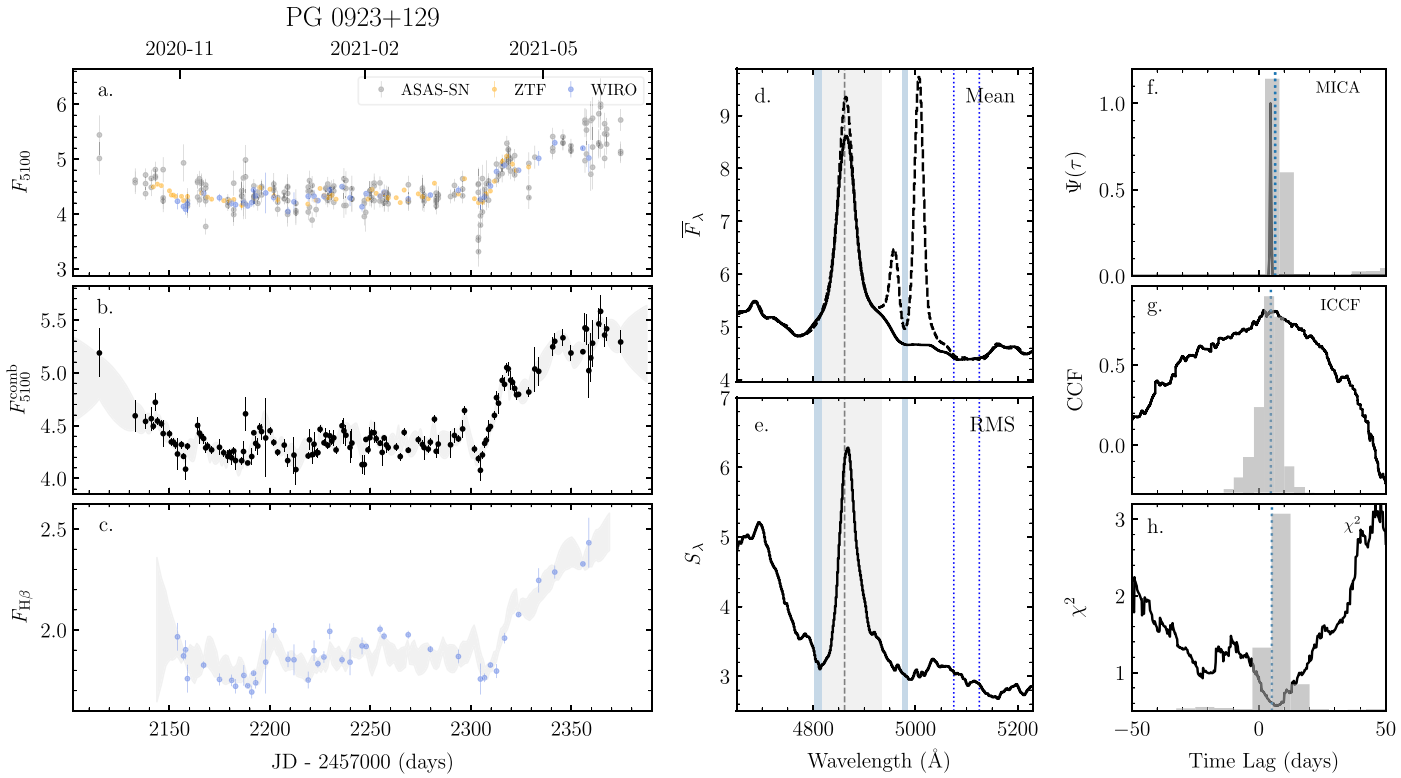

Figure 4. Time-series analysis of PG 0923+129. The meanings of the panels, lines, and histograms are the same as in Figure 2.

the idea that the apparent absorption effect is due the continuum contributions to the emission lines in the rms spectra.

3.2. Light Curves

The Hβ light curves can be measured by the direct integration method (e.g., Peterson et al. 1998; Kaspi et al. 2000; Bentz et al. 2009; Grier et al. 2012; Du et al. 2014) or spectral fitting methods (e.g., Barth et al. 2013; Hu et al. 2015). Paper I has described the advantages and disadvantages of these two methods and explained the reason why we decided to use the direct integration method in our MAHA campaign (see Section 3.1 there). As in Papers I and II, we adopted the integration method to measure the fluxes of the Hβ emission lines. The Hβ fluxes are measured after subtracting the underlying continuum. The continuum and the integration windows are selected according to the emission-line signals in the rms spectra but also to avoid the possible influence of the He II line and [O III] lines as much as possible. The narrow-line fluxes remaining in the integration windows are also included in the Hβ light curves. The 5100 Å continuum light curves are obtained by measuring the median fluxes density from 5075 to 5125 Å. The measurement windows for the continuum and Hβ are marked in the mean and rms spectra in Figures 2–16 for individual objects in different seasons. The light curves are provided in Table 5 and shown in Figures 2–16.

For some objects, the uncertainties described in Section 2 are still smaller than the apparent scatter in the light curves. This indicates that the changes of the weather, pointing, and tracking conditions on different nights have introduced some extra systematic uncertainties. We estimate these systematic uncertainties using the median-filter method (see more details in Du et al. 2014 or Paper I) and are provided in Table 4 as needed. In the following analysis, these systematic uncertainties are also included in the calculations by quadratic summation.

3.3. Intercalibration of Light Curves

Because of the different apertures used for the telescopes in our campaign (as well as ASAS-SN and ZTF) and the correspondingly different contributions from the host galaxies, we need to take care to properly intercalibrate the photometric and spectroscopic light curves. The intercalibration is performed by the Bayesian-based package PyCALI[26] (Li et al. 2014). It assumes that the light curves can be described by a damped random walk model and determines the best multiplicative and additive factors by exploring the posterior probability distribution with a diffusive-nested sampling algorithm (Brewer et al. 2011). The 5100 Å continuum and Hβ light curves from different telescopes are intercalibrated and then combined by averaging the observations during the same nights. The intercalibrated and combined light curves are shown in Figures 2–16. The light curves from different telescopes are generally quite consistent with each other. Several severely deviant data points differing from adjacent epochs and the MICA reconstruction (see below) or possessing significantly larger error bars are not included in the following time-series analysis in Figures 2–16.

In principle, the emission-line contributions (e.g., Hβ, Hγ, He II, Fe II) in the broad bands of photometric light curves may slightly influence the lag measurements. However, the broad-band photometric and spectroscopic (at 5100 Å) continuum light curves are all well consistent with each other in the present paper (see Figures 2–16), which means these influences can be ignored given the current uncertainties of the light

[26] PyCALI is available at: https://github.com/LiyrAstroph/PyCALI.

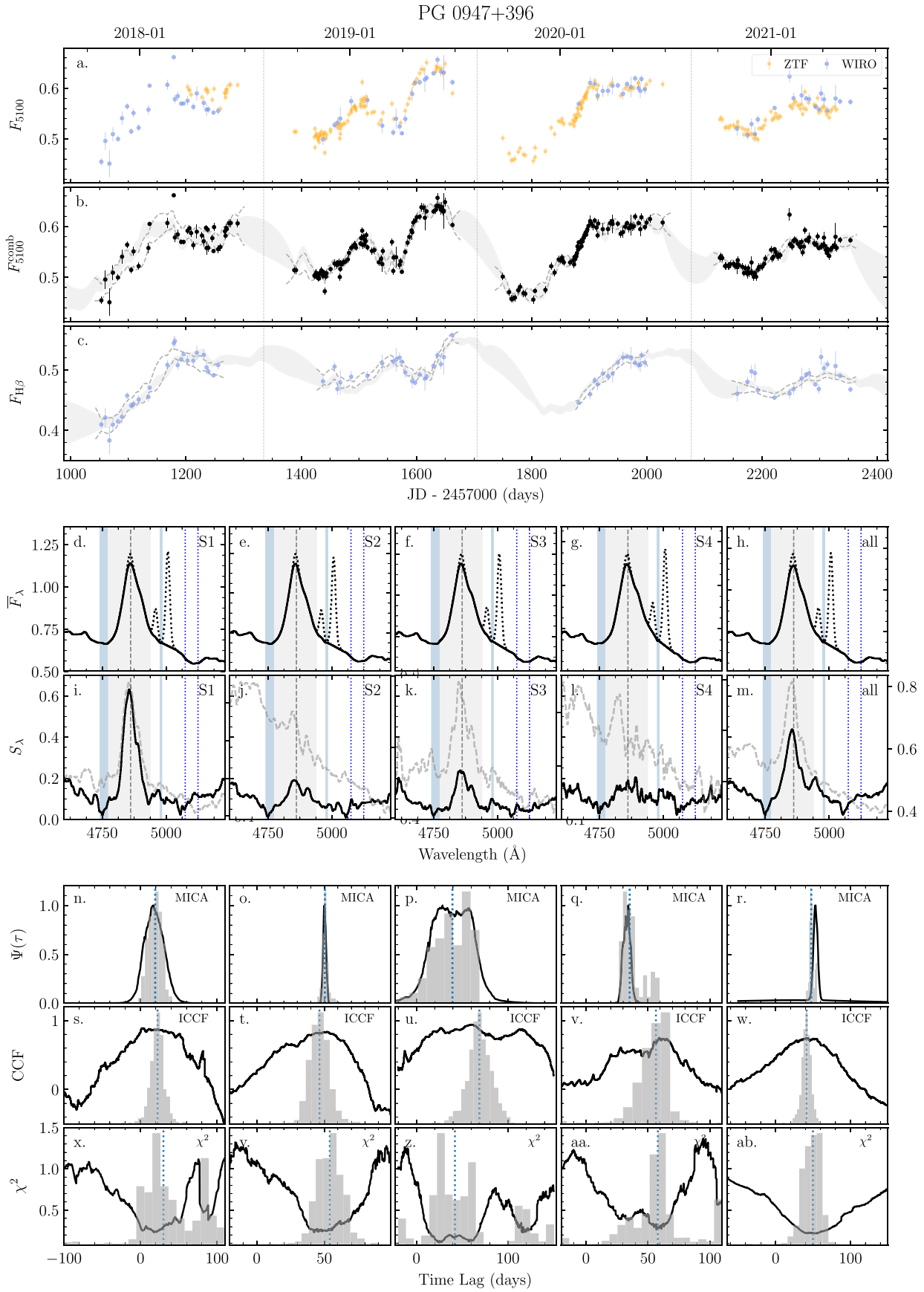

Figure 5. Time-series analysis of PG 0947+396. The gray and black dashed lines in panels (i)–(m) are the original and continuum-cleaned rms spectra (see more details in Section 3.1). The meanings of the other panels, lines, and histograms are the same as in Figure 2.

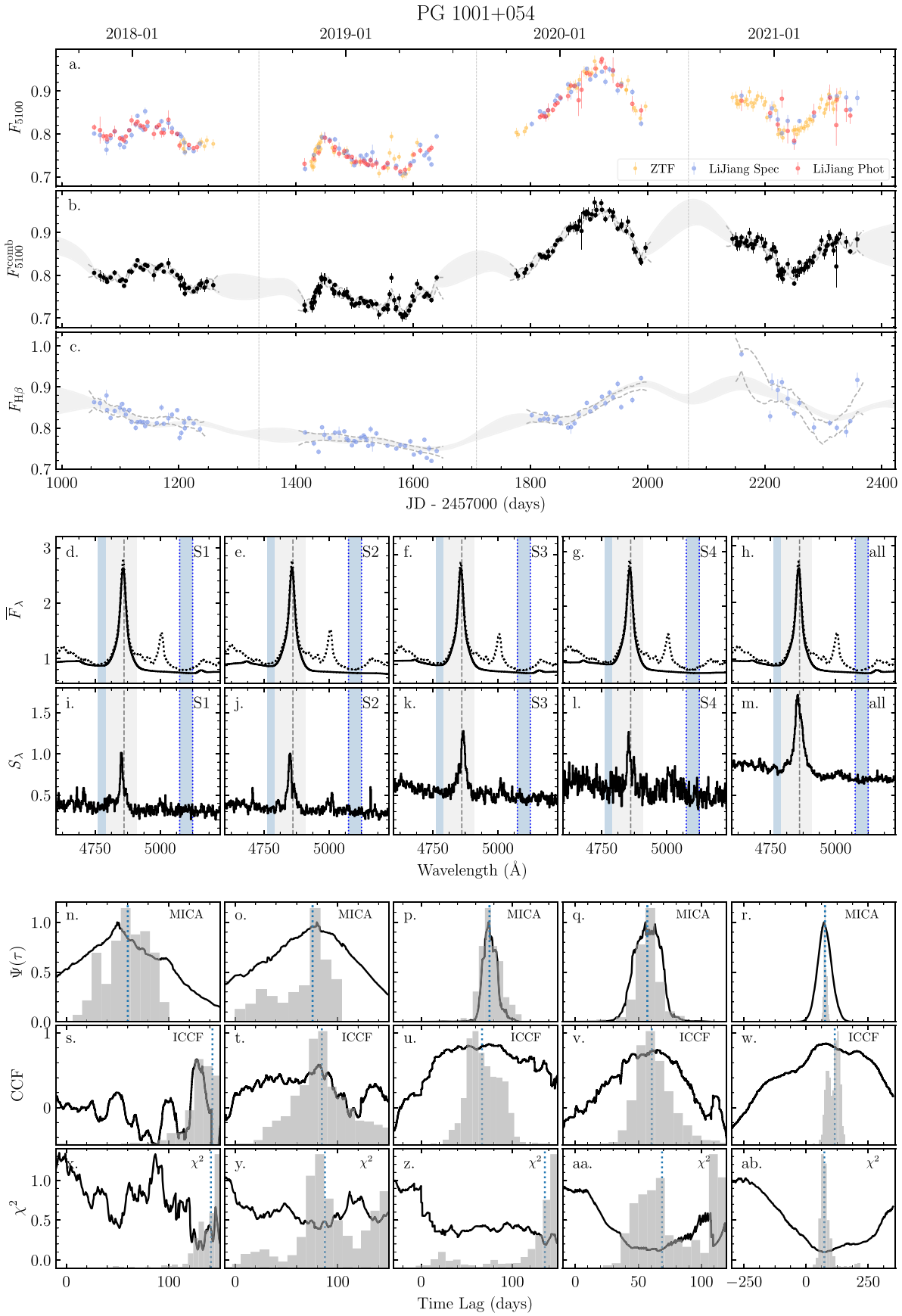

Figure 6. Time-series analysis of PG 1001+054. The black dotted and solid lines in panels (d)–(h) are the original and cleaned (e.g., Fe II, He II, narrow Hβ, and [O III]$\lambda\lambda$ 4959,5007) mean spectra. The meanings of the other panels, lines, and histograms are the same as in Figure 2.

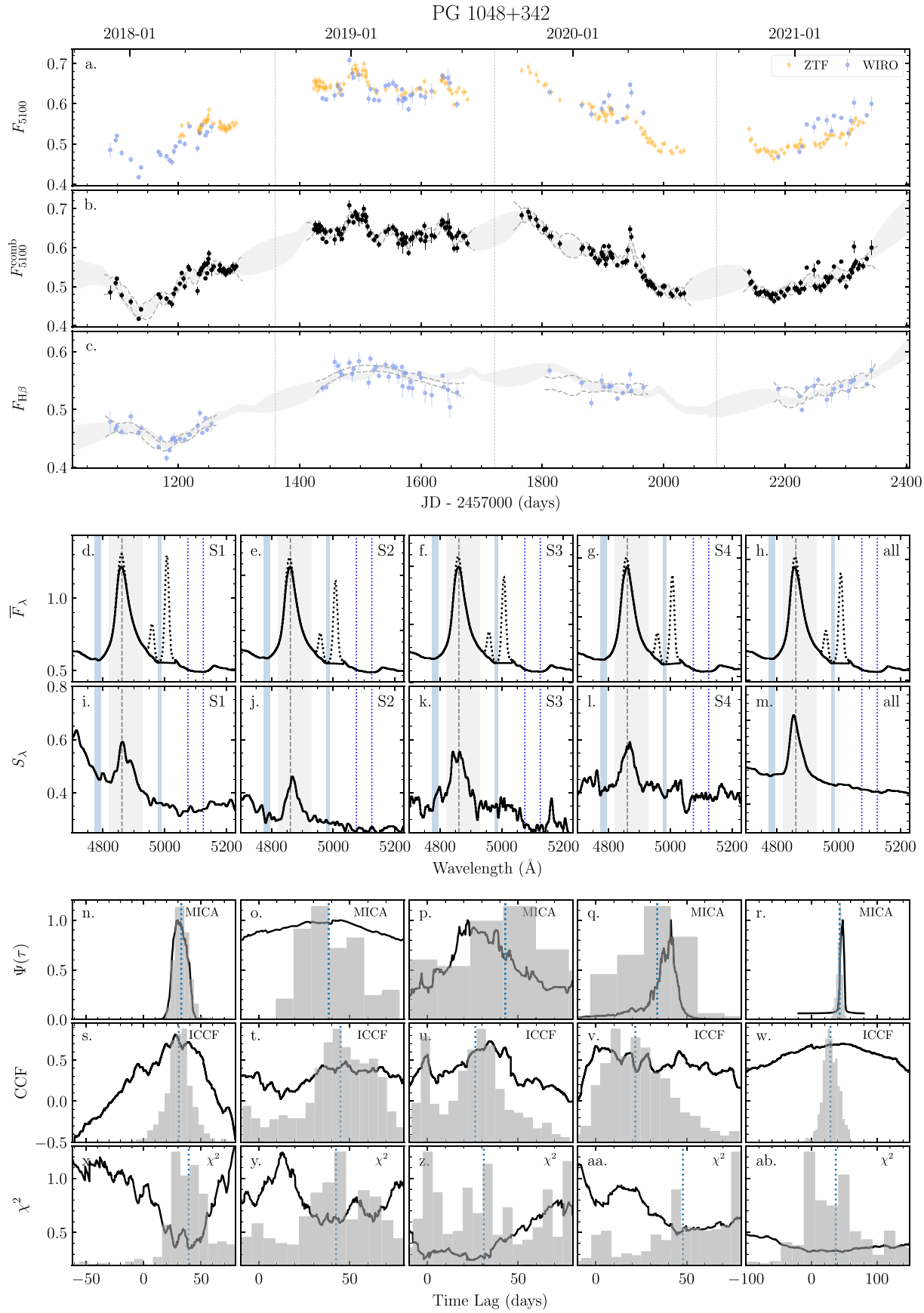

Figure 7. Time-series analysis of PG 1048+342. The meanings of the panels, lines, and histograms are the same as in Figure 2.

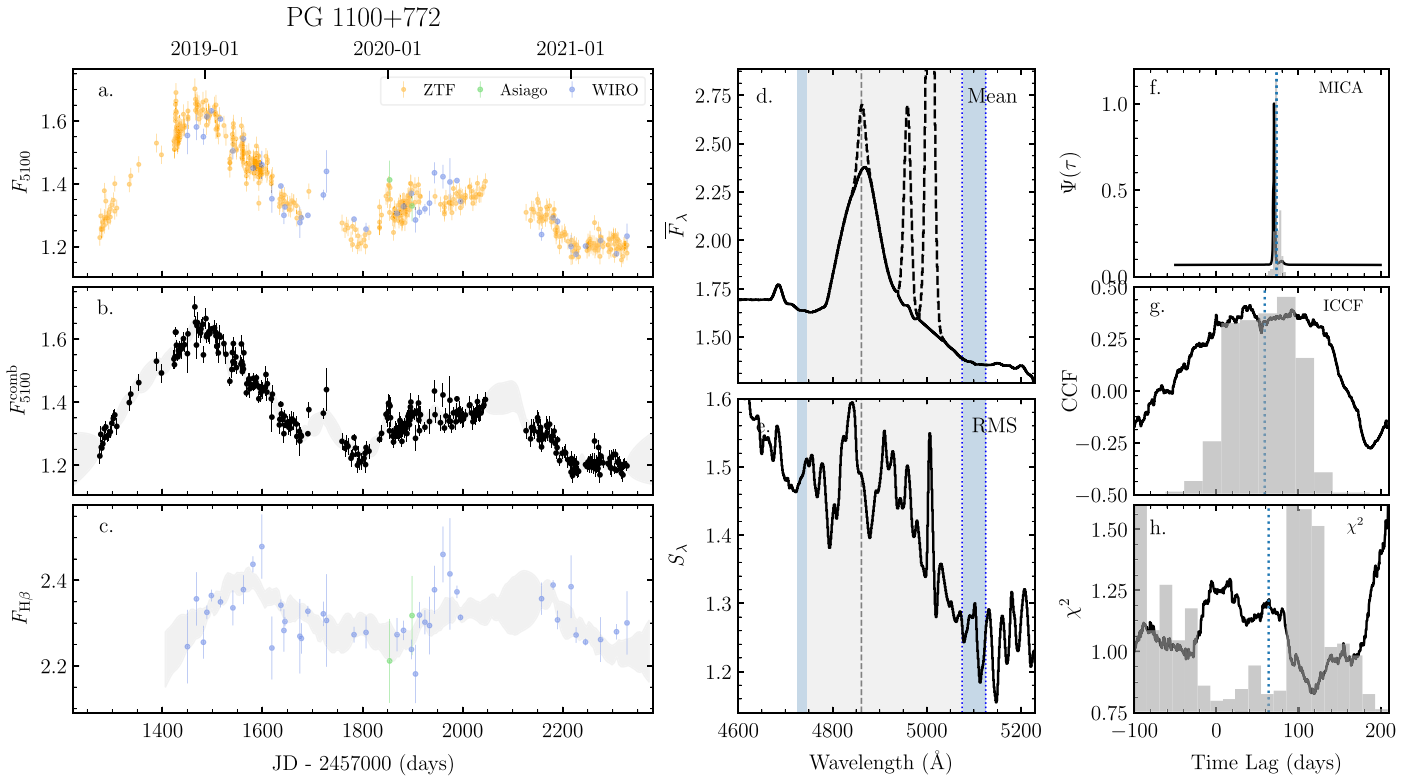

Figure 8. Time-series analysis of PG 1100+772. The meanings of the panels, lines, and histograms are the same as in Figure 2.

curves. This is very natural because the integrated emission-line fluxes in these broad bands are roughly smaller than 10% of the continuum fluxes and the emission-line variation amplitudes are generally smaller than those of the continuum (see Table 3).

The average fluxes and variability of the continuum and Hβ light curves are provided in Table 3. The variability and its uncertainty of a light curve have been defined (Rodríguez-Pascual et al. 1997; Edelson et al. 2002) as

$$F_{\rm var} = \frac{(\sigma^2 - \Delta^2)^{1/2}}{\langle F \rangle} \tag{4}$$

and

$$\sigma_{\rm Fvar} = \frac{1}{(2N)^{1/2} F_{\rm var}} \frac{\sigma^2}{\langle F \rangle^2}, \tag{5}$$

where σ is the mean square root of the variance, Δ^2 is the mean square value of the flux uncertainties, $\langle F \rangle$ is the average flux, and N is the number of epochs.

3.4. Line Width Measurements

The widths of the Hβ emission lines are measured from both the mean and rms spectra. Here, we use both FWHM and line dispersion $\sigma_{\rm H\beta}$ to quantify the line widths. For the rms spectra, the narrow emission lines (Hβ and [O III]$\lambda\lambda$ 4959,5007) are generally negligible. However, the Hβ and [O III] narrow emission lines in the mean spectra need to be removed before measuring the line widths of broad Hβ. The narrow Hβ lines were assumed to have the same profiles as the [O III] lines and were removed using the same local fitting method described in Paper I. The narrow-line subtracted spectra are shown in Figures 2–16.

However, the [O III]$\lambda\lambda$ 4959,5007 emission lines of PG 1202+281, PG1351+640, and PG 1351+695 are strongly blended with each other. In addition, PG 1001+054 and PG 1211+143 have strong Fe II emission lines. For these five objects, we make use of a more global fitting scheme to remove the contributions from the other emission lines (narrow Hβ, [O III], He II lines, and Fe II emission) before we measure the line widths of Hβ from the mean spectra. We adopted the software DASpec,[27] which is based on the Levenberg–Marquardt algorithm (Press et al. 1992), to perform the multicomponent fitting in a wide spectral range (4430–5550 Å). The fitting included (1) a power-law component for the continuum, (2) a template for Fe II emission (Boroson & Green 1992), (3) a simple stellar population template from Bruzual & Charlot (2003) for the contribution from host galaxy if necessary, (4) two Gaussians for broad Hβ, (5) one or two Gaussians for each of the narrow emission lines (e.g., Hβ and [O III]), and (6) one or two Gaussian for the He IIλ4686 line. The narrow lines were assumed to have the same profiles. The narrow Hβ lines in PG 1001+054 and PG 1211+143 are too weak to be decomposed from the broad Hβ. In their fitting, we fixed the flux of narrow Hβ to be 0.1 of their [O III]λ5007 lines.

We measured the line widths of the broad Hβ line in the mean spectra after removing the contributions of the other components (see Table 6). The cleaned mean spectra are shown in Figures 2–16. The uncertainties were estimated using the bootstrap method. A subset of N points were randomly extracted (with replacement) from the original N data points from the mean or rms spectrum. We repeated this procedure 500 times and measured the FWHM and $\sigma_{\rm H\beta}$ from the resampled spectra. The uncertainties were measured from the

[27] DASpec is available at https://github.com/PuDu-Astro/DASpec.

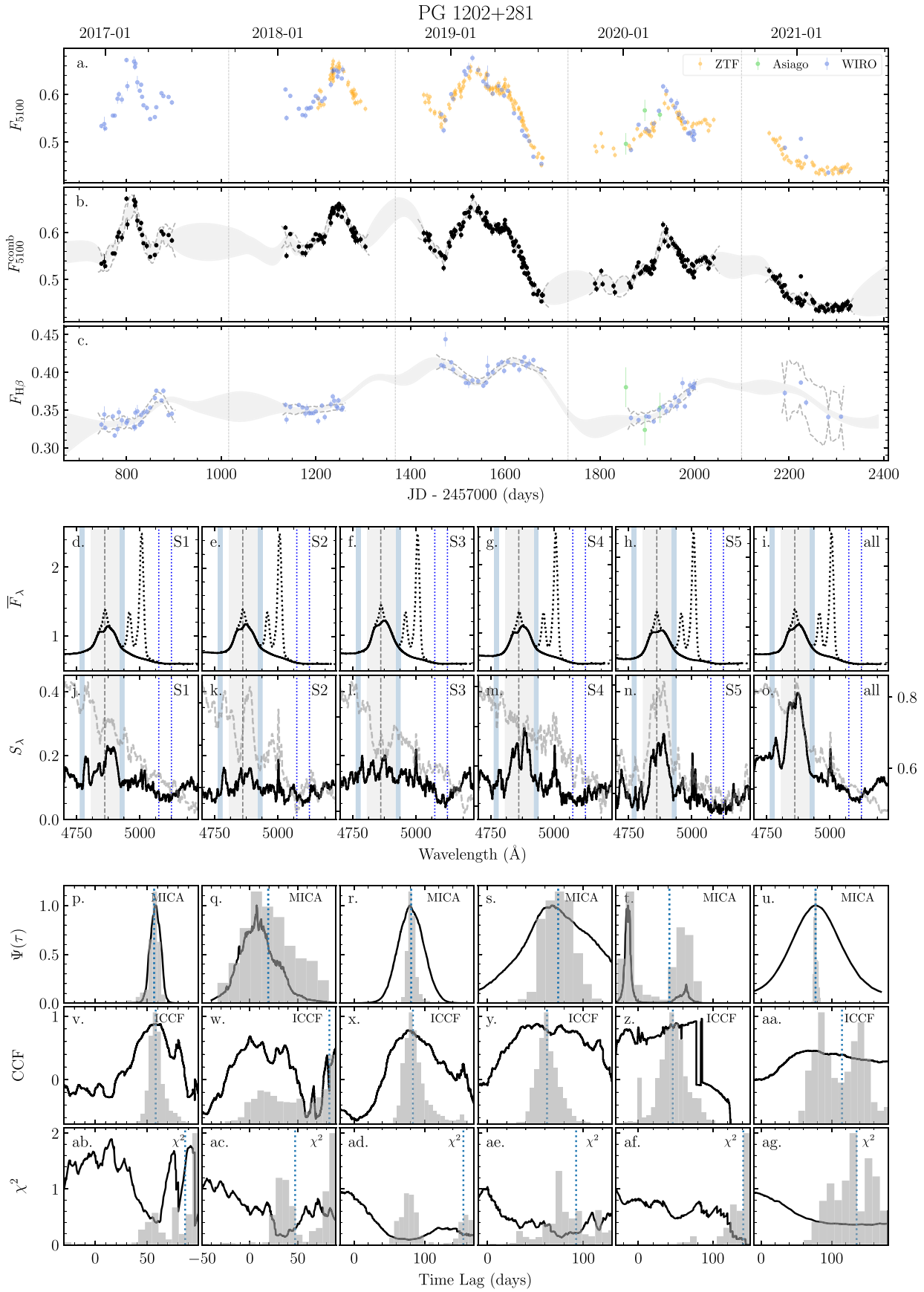

Figure 9. Time-series analysis of PG 1202+281. The meanings of the panels, lines, and histograms are the same as in Figure 2. In the narrow-line-correct mean spectra in panels (d)–(i).

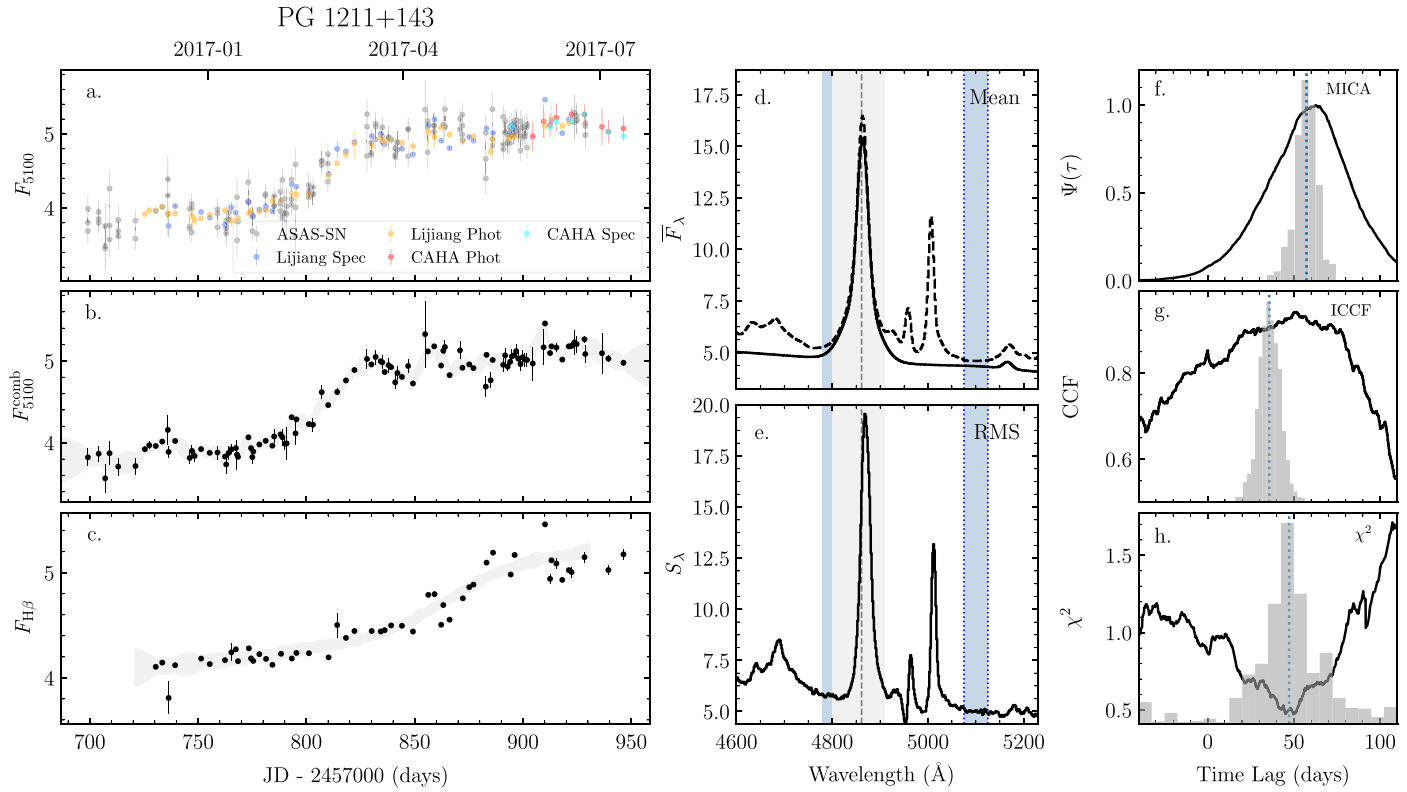

Figure 10. Time-series analysis of PG 1211+143. The black dotted and solid lines in panel (d) are the original and cleaned (e.g., Fe II, He II, narrow Hβ, and [O III]$\lambda\lambda$ 4959,5007) mean spectra. The meanings of the other panels, lines, and histograms are the same as in Figure 2. Panel (c) is the combined Hβ light curve from Lijiang and CAHA.

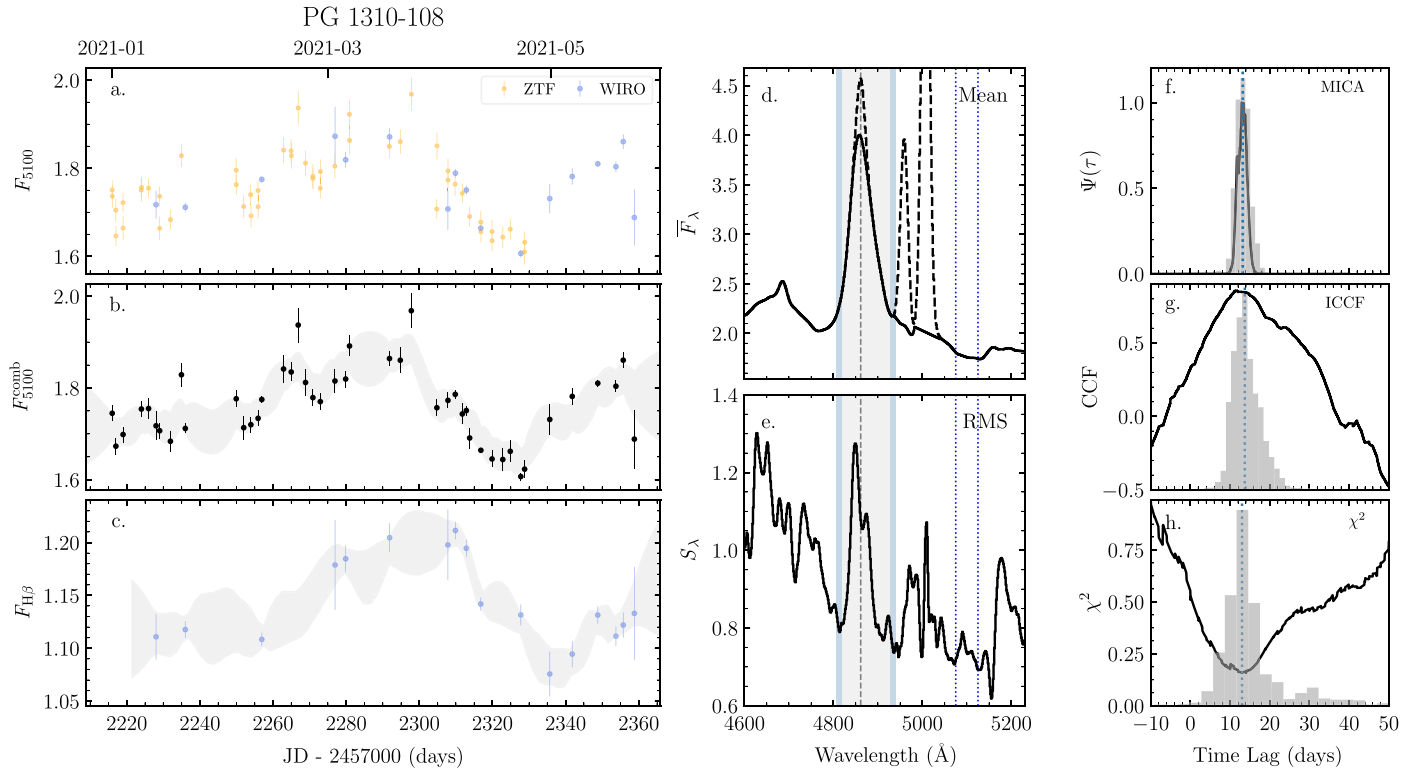

Figure 11. Time-series analysis of PG 1310−108. The meanings of the panels, lines, and histograms are the same as in Figure 2.

generated distributions. For PG 1001+054 and PG 1211+143, we estimated the uncertainties by assuming the flux ratio of narrow Hβ/[O III]λ5007 to be 0.0 and 0.2 (as aforementioned, the cases with Hβ/[O III] = 0.1 is assumed as the central value). This allowed us to take into account the uncertainties of narrow Hβ decomposition (see more details in Du et al. 2014).

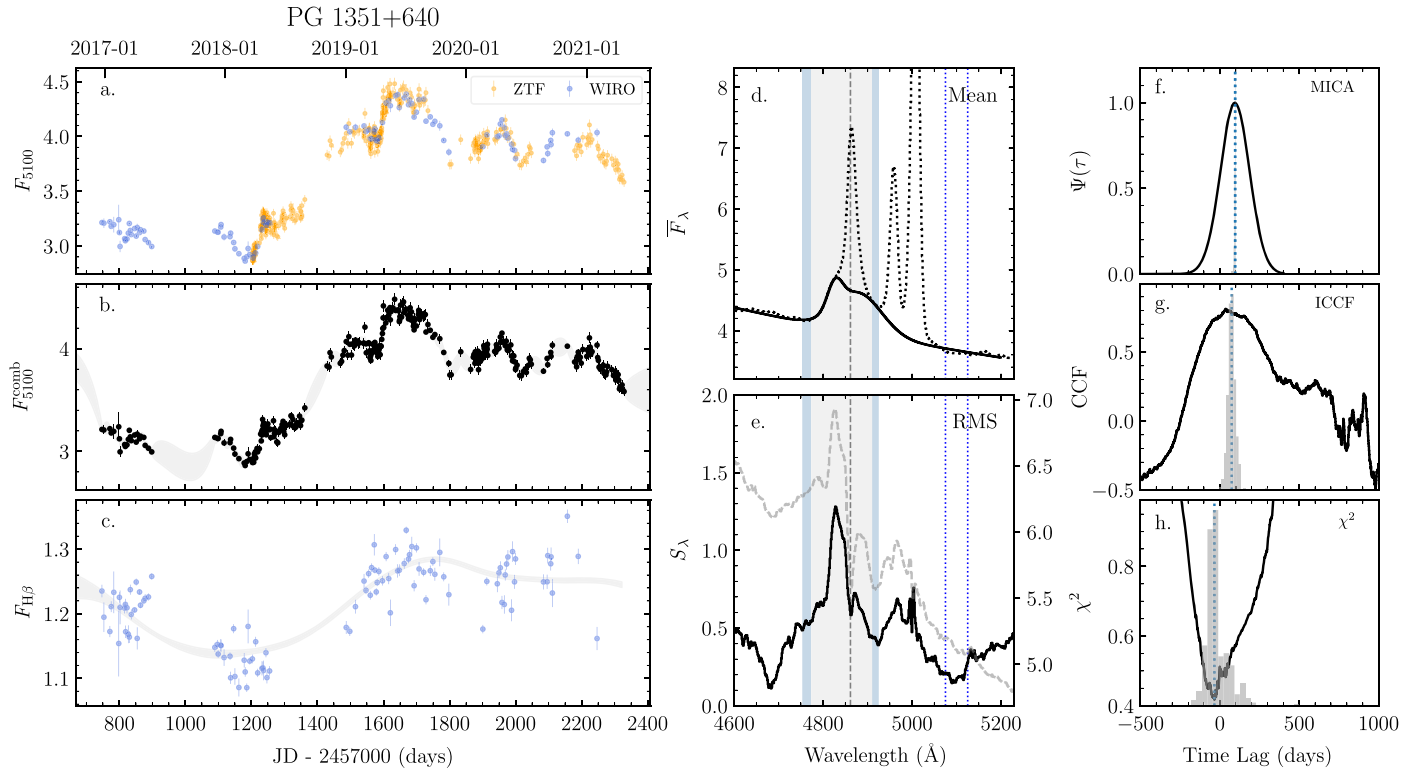

Figure 12. Time-series analysis of PG 1351+640. The black dotted and solid lines in panels (d)–(h) are the original and cleaned (e.g., Fe II, He II, narrow Hβ, and [O III]$\lambda\lambda$ 4959,5007) mean spectra. The meanings of the other panels, lines, and histograms are the same as in Figure 3.

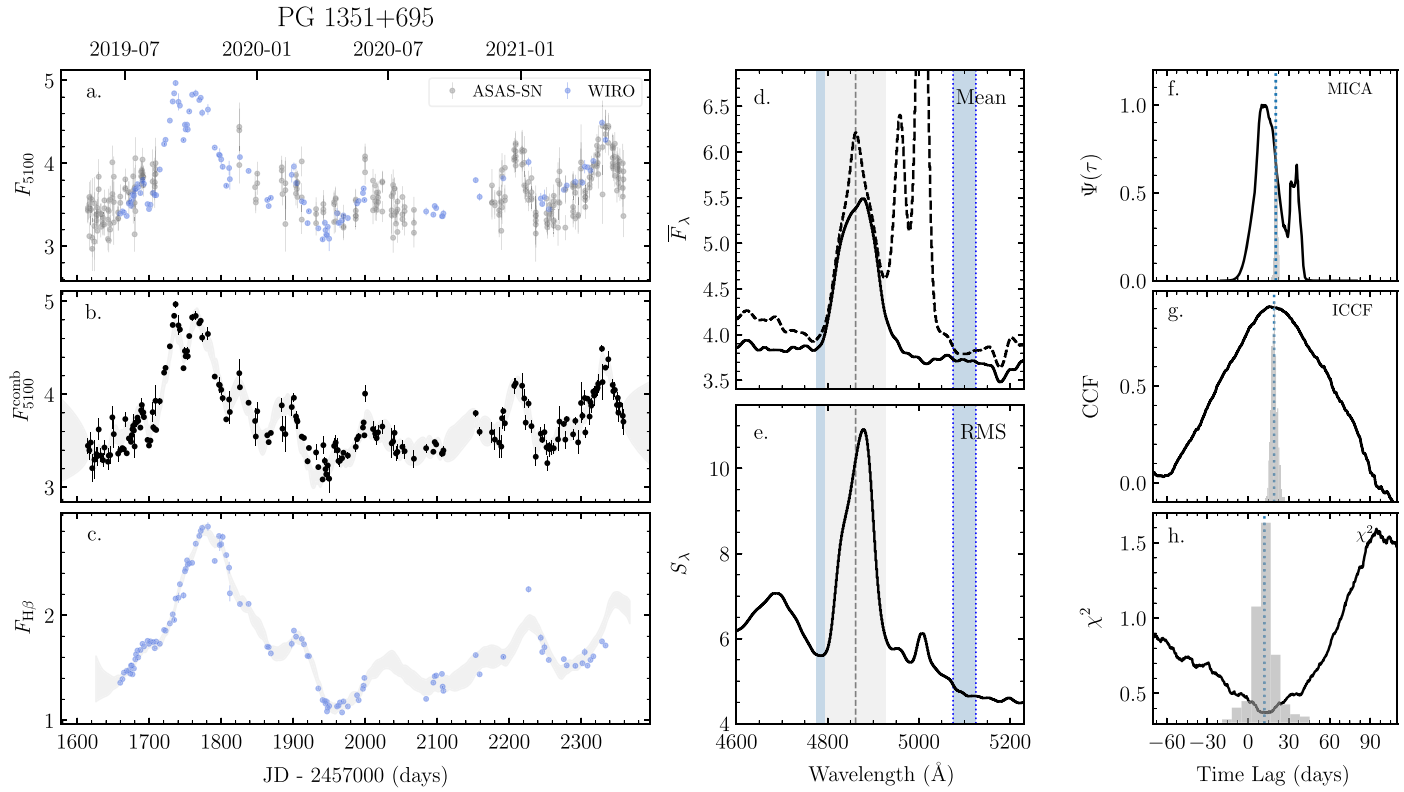

Figure 13. Time-series analysis of PG 1351+695. The meanings of the panels, lines, and histograms are the same as in Figure 2.

The FWHM and $\sigma_{H\beta}$ from the mean and rms spectra are provided in Table 6. The Hβ signal in the rms spectra of some objects is too weak for the line width measurement [PG 0049 +171 (Season 4), PG 0947+396 (Seasons 2 and 4), PG 1202 +281 (Seasons 1–4), PG 1351+640, PG 1501+106 (Season 2)]. We measured the FWHM and $\sigma_{H\beta}$ of Hβ from the aforementioned continuum-cleaned rms spectra for all seasons (see Section 3.1).

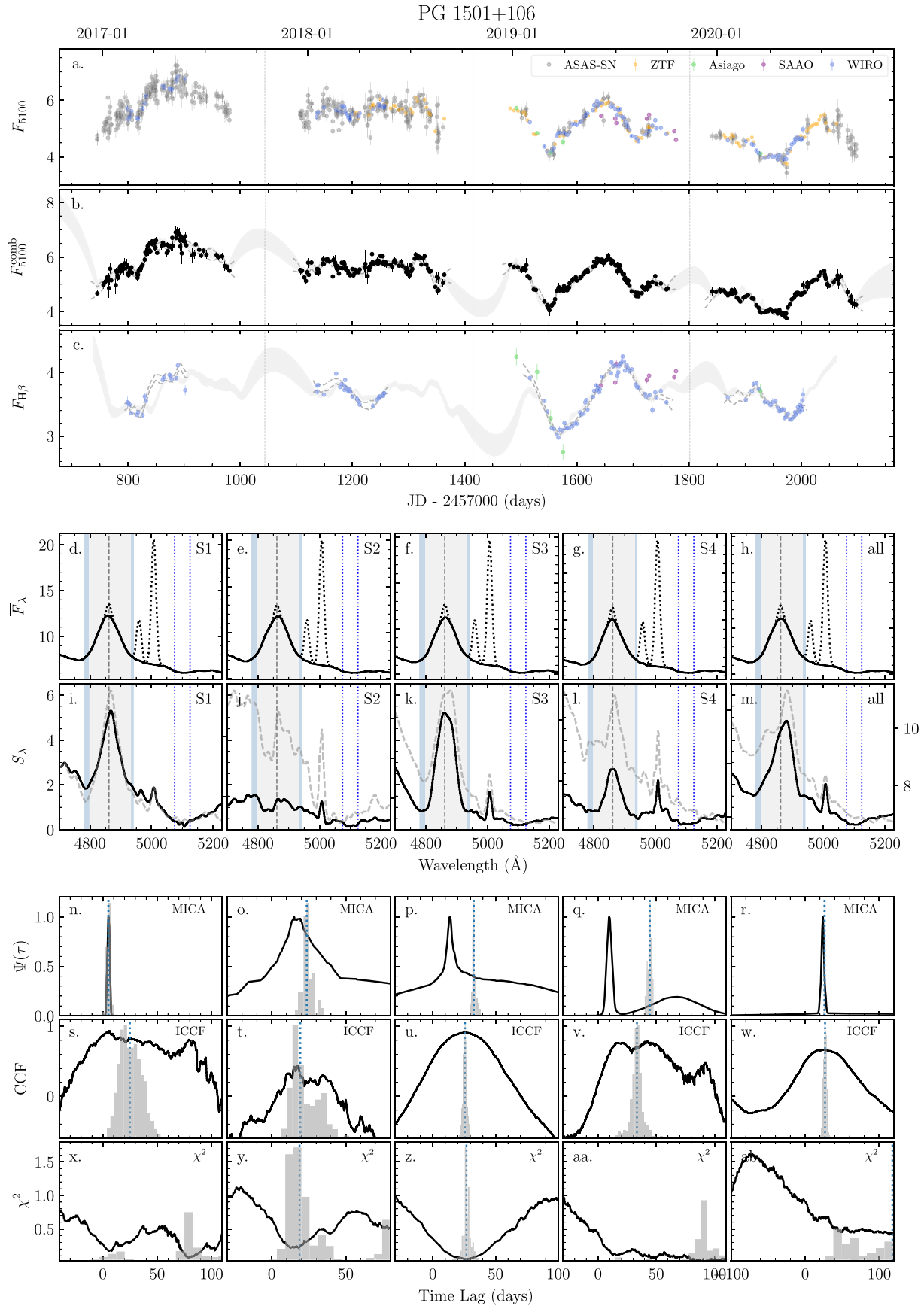

Figure 14. Time-series analysis of PG 1501+106. The meanings of the panels, lines, and histograms are the same as in Figure 3.

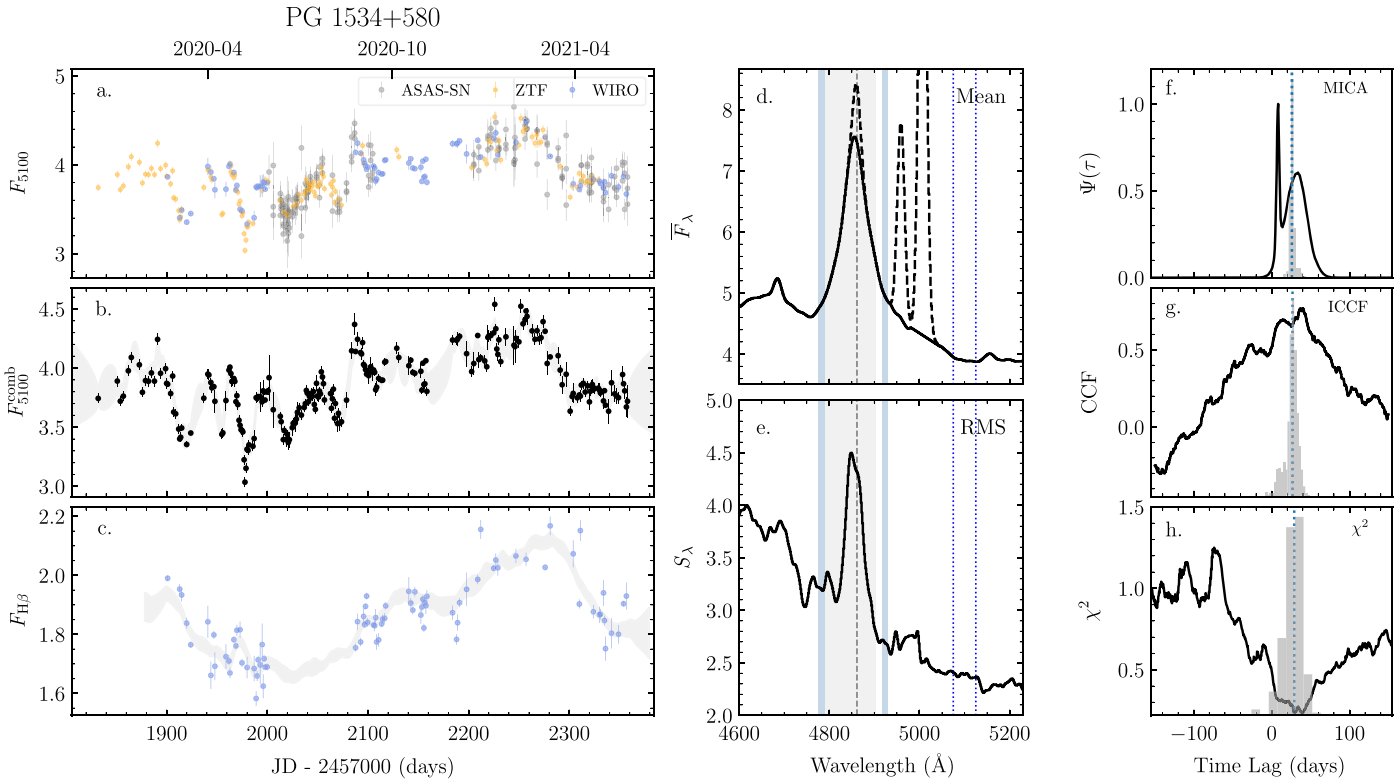

Figure 15. Time-series analysis of PG 1534+580. The meanings of the panels, lines, and histograms are the same as in Figure 2.

3.5. Time-series Analysis

We made use of three different methods to measure the Hβ time lags: the interpolated cross-correlation function (ICCF; Gaskell & Sparke 1986 and Gaskell & Peterson 1987), the χ^2 method (Czerny et al. 2013), and the MICA algorithm, which is a nonparametric approach to constrain the 1d transfer function in RM (Li et al. 2016). Here we briefly introduce the three methods for completeness. More details can be found in the references above.

ICCF: A commonly employed method in RM, we measured the time lags of Hβ using ICCF. In general, the time lags can be measured from the peak of the CCF and the centroid of the CCF above a threshold (80% of the peak), which are marked as $\tau_{\rm peak}$ and $\tau_{\rm cent}$, respectively. The uncertainties of the time lags were estimated using the "flux randomization/random subset sampling (FR/RSS)" method (Peterson et al. 1998, 2004). In the present paper, the median and 1σ limits of the cross-correlation centroid distributions (CCCDs) and the cross-correlation peak distributions generated by the FR/RSS method were adopted as the final lags and their uncertainties.

The χ^2 method: The χ^2 method (Czerny et al. 2013) was also employed to measure the time lags between the continuum and Hβ light curves. Czerny et al. (2013) found that the χ^2 method works better than using ICCF for the AGNs with red-noise variability. The technique takes into account the weights of the points in light curves through their uncertainties. After shifting and interpolating the Hβ light curves, the χ^2 were calculated by

$$\chi^2 = \frac{1}{N}\sum_{i=1}^{n}\frac{(x_i - A_{\chi^2} y_i)^2}{\delta x_i^2 + A_{\chi^2}^2 \delta y_i^2}, \tag{6}$$

where x_i and y_i are the continuum and interpolated Hβ fluxes, and δx_i and δy_i are their uncertainties. A_{χ^2} is a normalized factor formulated as

$$A_{\chi^2} = \frac{S_{xy} + (S_{xy}^2 + 4S_{x3y}S_{xy3})^{1/2}}{2S_{xy3}}, \tag{7}$$

where

$$\begin{aligned} S_{xy} &= \sum_{i=1}^{N}(x_i^2\delta y_i^2 - y_i^2\delta x_i^2), \\ S_{xy3} &= \sum_{i=1}^{N} x_i y_i \delta y_i^2, \\ S_{x3y} &= \sum_{i=1}^{N} x_i y_i \delta x_i^2. \end{aligned} \tag{8}$$

We took the minimum points in the χ^2 functions as the time-lag measurements. Similar to the ICCF method, the uncertainties were generated from FR/RSS as well.

MICA:[28] MICA (Li et al. 2016) is a Bayesian-based nonparameteric approach to infer the 1D transfer function from the continuum and emission-line light curves. It assumes that the transfer function is a sum of relatively displaced Gaussians and employs the diffusive-nested sampling technique to obtain posterior distributions of Gaussian parameters. For each set of parameters, we calculate the corresponding transfer function and obtain the centroid of the transfer function. The mean of the distribution of centroids is taken as the best estimate of the time lag and its uncertainty by the 68.3% confidence interval.

The CCFs and CCCDs, the χ^2 functions and their lag distributions, and the transfer functions and the corresponding

[28] MICA is available at https://github.com/LiyrAstroph/MICA2.

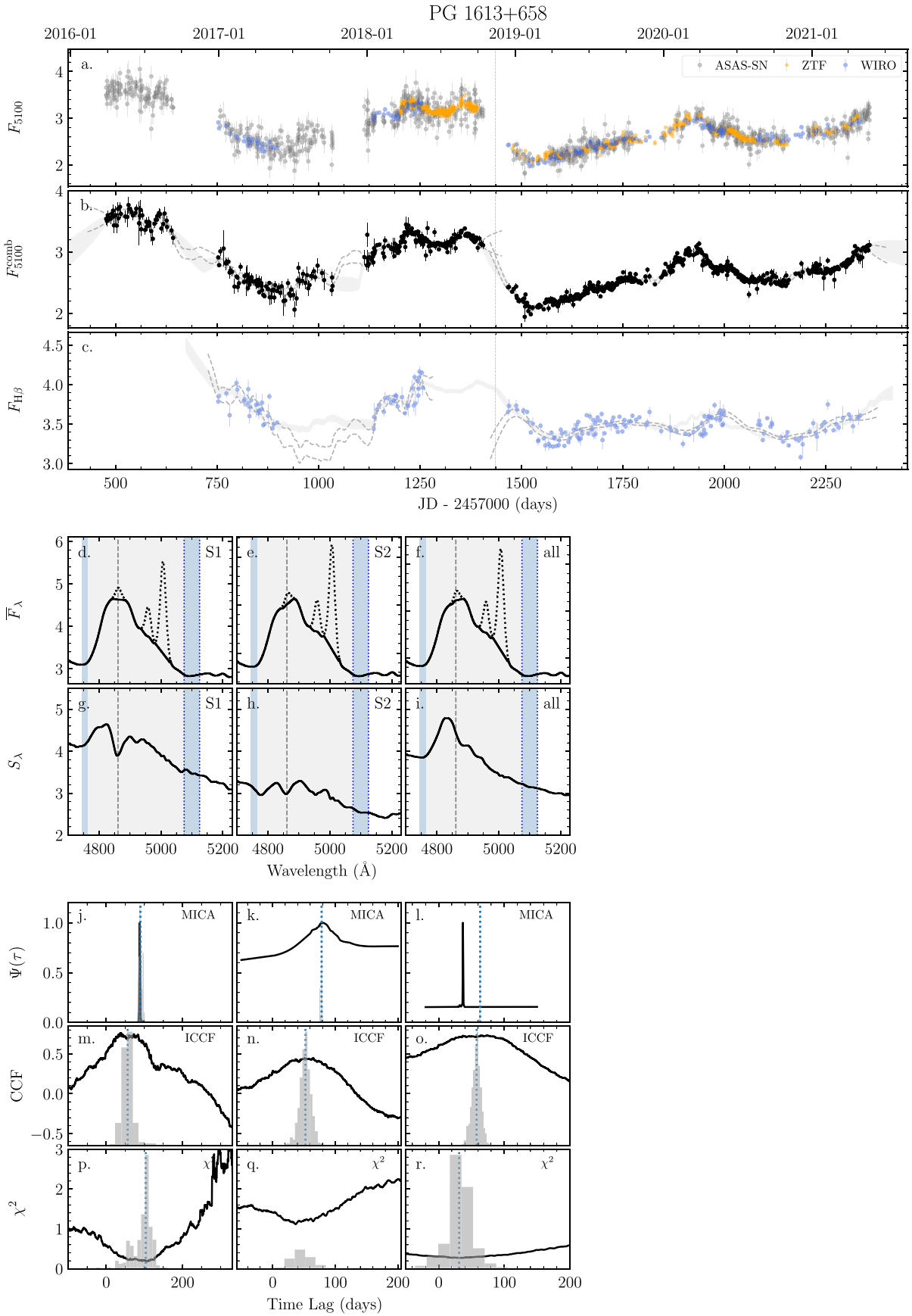

Figure 16. Time-series analysis of PG 1613+658. The meanings of the panels, lines, and histograms are the same as in Figure 2.

Table 3
Basic Information of Light Curves

Name	Spectroscopy			Continuum			Hβ	
	Season	Duration	Epochs	Cadence	F_{var} (%)	Flux density	F_{var}	Flux
				(days)		(%)		(%)
(1)	(2)	(3)	(4)	(5)	(6)	(7)	(8)	(9)
PG 0007+106	All	2017.10–2021.01	132	8.9	10.4 ± 0.7	0.95 ± 0.10	11.3 ± 0.7	1.51 ± 0.17
	1	2017.10–2018.01	23	4.3	7.5 ± 1.2	1.08 ± 0.08	5.5 ± 0.9	1.61 ± 0.09
	2	2018.08–2019.02	47	3.4	3.8 ± 0.5	0.95 ± 0.04	7.8 ± 0.9	1.64 ± 0.13
	3	2019.06–2020.02	35	6.5	11.3 ± 1.4	0.93 ± 0.11	8.2 ± 1.1	1.40 ± 0.12
	4	2020.08–2021.01	27	5.1	4.8 ± 0.9	0.86 ± 0.05	7.3 ± 1.1	1.35 ± 0.10
PG 0049+171	All	2017.10–2021.02	160	7.5	13.4 ± 0.8	1.77 ± 0.24	5.9 ± 0.4	1.88 ± 0.12
	1	2017.10–2018.02	28	4.5	6.4 ± 0.9	1.89 ± 0.13	7.2 ± 1.1	2.01 ± 0.15
	2	2018.08–2019.02	48	3.7	5.4 ± 0.6	1.50 ± 0.08	2.2 ± 0.4	1.78 ± 0.05
	3	2019.06–2020.02	44	5.5	8.9 ± 1.0	2.00 ± 0.18	3.3 ± 0.5	1.92 ± 0.08
	4	2020.08–2021.02	40	4.3	6.5 ± 0.8	1.74 ± 0.12	2.9 ± 0.5	1.85 ± 0.07
PG 0923+129	All	2020.10–2021.05	41	5.0	6.3 ± 0.8	4.41 ± 0.30	8.5 ± 1.0	1.90 ± 0.17
PG 0947+396	All	2017.10–2021.05	83	15.7	6.9 ± 0.6	0.57 ± 0.04	6.3 ± 0.6	0.49 ± 0.03
	1	2017.10–2018.05	26	7.8	7.5 ± 1.3	0.55 ± 0.05	9.7 ± 1.4	0.48 ± 0.05
	2	2018.11–2019.06	22	10.2	8.2 ± 1.3	0.57 ± 0.05	3.3 ± 0.8	0.50 ± 0.02
	3	2020.02–2020.05	16	7.2	1.1 ± 0.7	0.60 ± 0.01	4.3 ± 0.9	0.50 ± 0.02
	4	2020.11–2021.05	19	10.4	4.6 ± 1.0	0.56 ± 0.03	3.2 ± 0.8	0.48 ± 0.02
PG 1001+054	All	2017.10–2021.05	102	12.8	7.8 ± 0.6	0.81 ± 0.06	5.5 ± 0.4	0.81 ± 0.05
	1	2017.10–2018.04	31	5.8	2.6 ± 0.4	0.80 ± 0.02	2.4 ± 0.4	0.83 ± 0.02
	2	2018.10–2019.06	34	6.6	2.8 ± 0.4	0.75 ± 0.02	1.8 ± 0.5	0.77 ± 0.02
	3	2019.11–2020.05	23	8.1	4.3 ± 0.7	0.90 ± 0.04	3.5 ± 0.6	0.85 ± 0.03
	4	2020.11–2021.05	14	14.1	3.5 ± 0.9	0.85 ± 0.03	5.9 ± 1.4	0.86 ± 0.06
PG 1048+342	All	2017.11–2021.05	87	14.4	11.1 ± 0.9	0.58 ± 0.07	8.0 ± 0.7	0.52 ± 0.04
	1	2017.11–2018.05	23	7.3	5.8 ± 1.2	0.49 ± 0.03	3.4 ± 0.7	0.46 ± 0.02
	2	2018.11–2019.06	36	6.2	3.5 ± 0.6	0.63 ± 0.03	2.6 ± 0.6	0.56 ± 0.02
	3	2019.11–2020.04	13	11.9	2.3 ± 1.8	0.60 ± 0.03	1.3 ± 1.2	0.54 ± 0.02
	4	2020.12–2021.05	15	10.2	6.5 ± 1.5	0.55 ± 0.04	2.1 ± 0.8	0.54 ± 0.02
PG 1100+772	All	2018.11–2021.04	42	20.9	8.9 ± 1.0	1.37 ± 0.13	1.6 ± 0.5	2.32 ± 0.06
PG 1202+281	All	2016.12–2021.04	101	15.5	9.2 ± 0.7	0.58 ± 0.05	7.4 ± 0.6	0.37 ± 0.03
	1	2016.12–2017.05	26	5.7	6.4 ± 1.0	0.59 ± 0.04	3.7 ± 0.7	0.34 ± 0.02
	2	2018.01–2018.05	22	5.5	5.4 ± 0.9	0.60 ± 0.03	1.0 ± 0.8	0.35 ± 0.01
	3	2018.12–2019.07	27	7.8	10.1 ± 1.4	0.58 ± 0.06	2.6 ± 0.6	0.40 ± 0.01
	4	2020.01–2020.05	21	6.4	6.2 ± 1.0	0.54 ± 0.03	4.4 ± 0.8	0.36 ± 0.02
	5	2020.12–2021.04	5	23.8	6.3 ± 2.1	0.47 ± 0.03	5.3 ± 1.8	0.36 ± 0.02
PG 1211+143	All	2016.12–2017.07	52	4.2	12.1 ± 1.3	4.66 ± 0.58	10.3 ± 1.1	4.61 ± 0.50
PG 1310-108	All	2021.01–2021.05	17	7.7	3.3 ± 0.9	1.76 ± 0.08	3.3 ± 0.7	1.14 ± 0.04
PG 1351+640	All	2016.12–2021.02	109	13.8	14.1 ± 1.0	3.63 ± 0.51	4.7 ± 0.4	1.22 ± 0.06
PG 1351+695	All	2019.06–2021.04	108	6.2	12.2 ± 0.9	3.80 ± 0.47	26.9 ± 1.9	1.75 ± 0.48
PG 1501+106	All	2017.02–2020.06	136	8.9	13.2 ± 0.8	5.18 ± 0.69	7.6 ± 0.5	3.61 ± 0.28
	1	2017.02–2017.05	17	6.1	8.6 ± 1.6	6.06 ± 0.53	6.9 ± 1.2	3.67 ± 0.26
	2	2018.01–2018.05	28	4.3	2.9 ± 0.5	5.64 ± 0.18	2.7 ± 0.5	3.69 ± 0.11
	3	2019.02–2019.10	57	4.3	9.0 ± 0.9	5.20 ± 0.47	10.0 ± 1.0	3.64 ± 0.37
	4	2020.01–2020.06	34	3.9	7.2 ± 0.9	4.34 ± 0.32	4.1 ± 0.5	3.47 ± 0.15
PG 1534+580	All	2020.02–2021.05	83	5.5	5.8 ± 0.5	3.90 ± 0.24	6.0 ± 0.6	1.85 ± 0.12
PG 1613+658	All	2016.12–2021.04	200	7.9	11.9 ± 0.6	2.62 ± 0.32	5.1 ± 0.3	3.55 ± 0.20
	1	2016.12–2018.05	55	9.2	12.2 ± 1.2	2.84 ± 0.35	3.7 ± 0.5	3.78 ± 0.17
	2	2018.12–2021.04	145	6.0	10.0 ± 0.6	2.53 ± 0.26	3.0 ± 0.3	3.46 ± 0.13

Note. Column 1 is the name of object. Column 2 is the season for the measurement. Columns 3–5 are the duration, epoch, and cadence of the spectroscopy. Columns 6–7 are the variation amplitude and mean flux for the continuum light curve. The uncertainty range of the mean flux is the standard deviation of the light curve. The unit of the mean flux is 10^{-15} erg s^{-1} cm^{-2} Å^{-1}. Columns 8–9 are the variation amplitude and mean flux for the Hβ light curve. The unit of the mean flux is 10^{-13} erg s^{-1} cm^{-2}.

uncertainties generated from MICA are shown in Figures 2–16. The time lags and their uncertainties are given in Table 6. For the light curves with clear variations and statistically significant time delays (e.g., Season 4 of PG 0049+171; Season 2 of PG 0947+396, PG 1310−108), the measurements of the three methods are generally consistent with each other. The pairwise comparison between the lag measurements of the methods are demonstrated in Figure 17. The results from ICCF and MICA have the best consistency, while the χ^2 method generally gives larger scatter compared to the other two methods. Considering that MICA takes advantage of a damped random walk model (Li et al. 2016) and can give better constraints to the light-curve reconstruction by incorporating the continuum and Hβ variations, in particular across larger gaps, we adopted the time lags from MICA for the BH mass measurements in the following Section 3.6.

Table 4
Systematic Errors of Light Curves

Target	Duration	σ_{sys} (conti)	σ_{sys} (Hβ)
PG 0007+106	2017.10–2018.01	0.019	0.026
PG 0007+106	2018.08–2019.02	0.015	0.031
PG 0007+106	2019.06–2020.02	0.022	0.034
PG 0007+106	2020.08–2021.01	0.022	0.026
PG 0049+171	2017.10–2018.02	0.037	0.042
PG 0049+171	2018.08–2019.02	0.014	0.028
PG 0049+171	2019.06–2020.02	0.030	0.043
PG 0049+171	2020.08–2021.02	0.021	0.038
PG 0923+129	2020.10–2021.05	0.000	0.000
PG 0947+396	2017.10–2018.05	0.017	0.009
PG 0947+396	2018.11–2019.06	0.003	0.000
PG 0947+396	2020.02–2020.05	0.000	0.000
PG 0947+396	2020.11–2021.05	0.009	0.000
PG 1001+054	2017.10–2018.04	0.010	0.011
PG 1001+054	2018.10–2019.06	0.007	0.013
PG 1001+054	2019.11–2020.05	0.009	0.013
PG 1001+054	2020.11–2021.05	0.011	0.020
PG 1048+342	2017.11–2018.05	0.017	0.007
PG 1048+342	2018.11–2019.06	0.005	0.007
PG 1048+342	2019.11–2020.04	0.022	0.010
PG 1048+342	2020.12–2021.05	0.013	0.004
PG 1100+772	2018.11–2019.09	0.000	0.000
PG 1100+772	2019.10–2020.05	0.000	0.000
PG 1100+772	2020.11–2021.04	0.017	0.000
PG 1202+281	2016.12–2017.05	0.014	0.007
PG 1202+281	2018.01–2018.05	0.012	0.006
PG 1202+281	2018.12–2019.07	0.009	0.007
PG 1202+281	2020.01–2020.05	0.008	0.006
PG 1202+281	2020.12–2021.04	0.007	0.004
PG 1211+143	2016.12–2017.07	0.148	0.146
PG 1310-108	2021.01–2021.05	0.038	0.000
PG 1351+640	2016.12–2017.05	0.000	0.020
PG 1351+640	2017.12–2018.05	0.020	0.021
PG 1351+640	2019.01–2019.11	0.049	0.021
PG 1351+640	2020.02–2020.05	0.002	0.025
PG 1351+640	2020.08–2021.02	0.036	0.030
PG 1351+695	2019.06–2020.05	0.061	0.036
PG 1351+695	2020.08–2021.04	0.108	0.136
PG 1501+106	2017.02–2017.05	0.098	0.043
PG 1501+106	2018.01–2018.05	0.056	0.048
PG 1501+106	2019.02–2019.10	0.041	0.046
PG 1501+106	2020.01–2020.06	0.000	0.019
PG 1534+580	2020.02–2020.05	0.037	0.029
PG 1534+580	2020.08–2021.05	0.070	0.051
PG 1613+658	2016.12–2017.05	0.022	0.083
PG 1613+658	2018.01–2018.05	0.000	0.000
PG 1613+658	2018.12–2020.05	0.027	0.058
PG 1613+658	2020.08–2021.04	0.027	0.048

Note. These are the systematic errors of the spectroscopy data in separate seasons. The systematic error of "0.000" means that it can be ignored. For PG 1100+772, PG 1351+640, PG 1351+695, PG 1534+580, and PG 1613+658, we did not divide their light curves into different seasons according to their gaps in the campaign because of the long variation timescales (see details in Section 2.2). However, their systematic uncertainties for continuum and Hβ used in the time-series analysis in Section 3 are estimated in light of the gaps in the campaign (if necessary). The unit for continuum systematic errors is 10^{-15} erg s^{-1} cm^{-2} Å^{-1}. The unit for Hβ systematic errors is 10^{-13} erg s^{-1} cm^{-2}.

3.6. Black Hole Masses

Given the time lag and the line width measurements, the BH masses $M_\bullet$ can be determined by the formula

$$M_\bullet = f_{\rm BLR}\frac{R_{\rm BLR}V^2}{G}, \quad (9)$$

where $R_{\rm BLR} = c\tau_{\rm BLR}$ is the responsivity-weighted radius of the BLR, $\tau_{\rm BLR}$ is the time lag, c is the speed of light, V is $\sigma_{\rm H\beta}$ or FWHM of the Hβ line from the mean or rms spectra, G is the gravitational constant, and $f_{\rm BLR}$ is a scaling factor.

The average value of $f_{\rm BLR}$ for AGNs as a sample can be determined by calibration against the $M_\bullet$–σ_* or $M_\bullet$–M_* relationships of inactive galaxies (e.g., Onken et al. 2004; Woo et al. 2010, 2015; Ho & Kim 2014), where σ_* and M_* are the stellar velocity dispersion and stellar mass of the galactic bulge. However, the specific values of $f_{\rm BLR}$ in individual objects are likely to have a significant scatter around the average (e.g., Pancoast et al. 2014; Grier et al. 2017; Li et al. 2018; Williams et al. 2018). Here we adopt the calibrated average $f_{\rm BLR}$ from Woo et al. (2015; 1.12 for FWHM and 4.47 for $\sigma_{\rm H\beta}$) in our $M_\bullet$ calculations, as we did for Papers I and II.

It has been suggested that the line widths in the rms spectra and time lags are more consistent with the virial relationship ($\tau \propto V^{-2}$) than the mean spectra (e.g., Peterson et al. 2004; Dalla Bontà et al. 2020). Therefore, we calculated the BH masses using the line widths from the rms spectra. But for completeness, we provided the "virial products (VP)" measured from the FWHM of the mean spectra ($R_{\rm H\beta}V^2_{\rm FWHM}/G$). We divided the light curves of the objects according to their seasonal gaps and measured the time lags for different seasons (Section 2.2) as well as for combined seasons. Table 7 gives the corresponding VP measured from the mean spectra, as well as BH masses ($f_{\rm BLR}R_{\rm BLR}V^2/G$) measured from the FWHM and $\sigma_{\rm H\beta}$ of the rms spectra; seasons with very poor lag measurements are ignored in the mass determinations. For completeness, the monochromatic luminosity at 5100 Å is available in Table 6. It should be noted that we have corrected for the Galactic extinction, but host-galaxy contamination is present in these measurements. We will investigate the location of our targets on the radius–luminosity plane (e.g., Kaspi et al. 2000; Bentz et al. 2013; Du & Wang 2019) in a future paper. The cosmological parameters used to calculate the luminosity are $H_0 = 67$ km s^{-1} Mpc^{-1}, $\Omega_M = 0.32$, $\Omega_\Lambda = 0.68$ (Planck Collaboration et al. 2014, 2020).

The time lags can vary over time, for instance if there are strong luminosity changes. In principle, it should not make a difference to the measurement of BH mass if we use the time lag from the light curves of any individual season or from the entire campaign, as the BH mass cannot change on short timescales. In practice, some seasons have stronger variations and better sampling than others. However, if the BLR kinematics is complex or variable, the BH masses measured from individual seasons or the whole

Table 5
Light Curves

Target	Telescope	Data	JD	Flux
PG 0007+106	WIRO	Conti	1046.674	0.982 ± 0.004
PG 0007+106	WIRO	Hβ	1046.674	1.501 ± 0.007
PG 0007+106	WIRO	Conti	1049.699	0.963 ± 0.004
PG 0007+106	WIRO	Hβ	1049.699	1.519 ± 0.006
PG 0007+106	WIRO	Conti	1050.721	0.985 ± 0.005
PG 0007+106	WIRO	Hβ	1050.721	1.473 ± 0.008

Note. The uncertainty does not include the systematic errors measured from median-filter method (see Section 3.2). The Julian dates are from 2,457,000. The units for continuum and Hβ are 10^{-15} erg s^{-1} cm^{-2} Å^{-1} and 10^{-13} erg s^{-1} cm^{-2}, respectively.

(This table is available in its entirety in machine-readable form.)

Table 6
Line Widths, Time Lags in the Rest Frame, and 5100 Å Luminosity

Target	Mean Spectra		rms		ICCF		MICA	χ^2		λL_λ(5100 Å)
	Season	FWHM (km s^{-1})	$\sigma_{\rm line}$ (km s^{-1})	FWHM (km s^{-1})	$\sigma_{\rm line}$ (km s^{-1})	$\tau_{\rm cent}$ (days)	$\tau_{\rm peak}$ (days)	$\tau_{\rm cent}$ (days)	$\tau_{\rm peak}$ (days)	($\times 10^{44}$ erg s^{-1})
PG 0007+106	All	5301^{+33}_{-28}	2424^{+39}_{-41}	4832^{+10}_{-11}	1766^{+11}_{-9}	$30.9^{+2.5}_{-2.4}$	$25.1^{+1.9}_{-4.4}$	$25.8^{+1.2}_{-1.1}$	$24.2^{+3.8}_{-3.2}$	1.61 ± 0.17
	1	5365^{+28}_{-28}	2524^{+43}_{-44}	5396^{+25}_{-24}	1895^{+21}_{-21}	$22.1^{+7.8}_{-5.7}$	$19.5^{+24.3}_{-4.0}$	$23.3^{+6.2}_{-4.0}$	$51.2^{+7.8}_{-32.9}$	1.84 ± 0.14
	2	5244^{+33}_{-30}	2347^{+34}_{-34}	4621^{+7}_{-6}	1881^{+13}_{-14}	$34.7^{+4.0}_{-4.3}$	$32.0^{+5.6}_{-7.6}$	$19.7^{+9.3}_{-13.7}$	$15.0^{+4.4}_{-2.7}$	1.62 ± 0.07
	3	5433^{+44}_{-29}	2365^{+41}_{-37}	4471^{+29}_{-29}	1750^{+24}_{-24}	$15.6^{+15.4}_{-11.1}$	$14.4^{+4.5}_{-6.0}$	$14.3^{+2.5}_{-2.6}$	$4.6^{+19.3}_{-150.2}$	1.58 ± 0.18
	4	5176^{+37}_{-24}	2558^{+56}_{-53}	4686^{+9}_{-10}	1558^{+14}_{-12}	$25.1^{+10.4}_{-6.7}$	$20.7^{+6.9}_{-3.8}$	$20.8^{+2.1}_{-2.0}$	$98.2^{+9.8}_{-12.9}$	1.45 ± 0.08
PG 0049+171	All	4262^{+411}_{-38}	2272^{+38}_{-32}	2873^{+7}_{-4}	1193^{+13}_{-13}	$34.7^{+3.8}_{-4.5}$	$28.1^{+11.4}_{-5.5}$	$39.5^{+3.3}_{-2.6}$	$84.9^{+43.7}_{-31.4}$	1.27 ± 0.17
	1	4131^{+394}_{-48}	2005^{+45}_{-46}	2804^{+9}_{-17}	1109^{+17}_{-21}	$51.2^{+3.7}_{-3.8}$	$54.2^{+5.2}_{-9.9}$	$41.8^{+7.2}_{-6.3}$	$31.8^{+20.9}_{-20.6}$	1.36 ± 0.09
	2	4426^{+399}_{-95}	2309^{+37}_{-42}	2919^{+13}_{-8}	1370^{+14}_{-13}	$23.7^{+14.0}_{-4.4}$	$22.2^{+9.4}_{-4.6}$	$30.9^{+3.7}_{-7.6}$	$27.1^{+36.8}_{-9.5}$	1.07 ± 0.06
	3	4296^{+311}_{-47}	2333^{+36}_{-32}	1896^{+9}_{-7}	988^{+21}_{-19}	$33.0^{+6.7}_{-9.3}$	$34.6^{+5.1}_{-11.4}$	$46.3^{+64.3}_{-8.6}$	$28.2^{+13.3}_{-10.3}$	1.44 ± 0.13
	4	4222^{+478}_{-42}	2327^{+52}_{-36}	3425^{+12}_{-13}	1223^{+19}_{-23}	$20.4^{+4.0}_{-3.4}$	$20.6^{+4.4}_{-3.6}$	$22.6^{+2.7}_{-2.2}$	$20.3^{+7.7}_{-5.2}$	1.25 ± 0.08
PG 0923+129	All	2461^{+34}_{-34}	1711^{+51}_{-48}	2138^{+17}_{-13}	1215^{+20}_{-19}	$4.6^{+3.4}_{-4.8}$	$5.5^{+1.6}_{-3.7}$	$6.2^{+3.2}_{-1.8}$	$5.0^{+4.5}_{-90.5}$	0.56 ± 0.04
PG 0947+396	All	5440^{+24}_{-76}	2872^{+33}_{-27}	3292^{+28}_{-33}	2021^{+27}_{-32}	$34.4^{+4.5}_{-4.9}$	$36.3^{+8.4}_{-8.9}$	$39.5^{+3.8}_{-1.7}$	$41.4^{+6.8}_{-10.8}$	5.85 ± 0.43
	1	5222^{+44}_{-24}	2797^{+36}_{-33}	3757^{+28}_{-37}	1653^{+26}_{-29}	$18.4^{+6.0}_{-6.8}$	$17.4^{+15.5}_{-14.1}$	$15.9^{+7.0}_{-7.8}$	$24.8^{+44.7}_{-18.9}$	5.68 ± 0.47
	2	5156^{+68}_{-24}	2816^{+33}_{-27}	5002^{+15}_{-16}	1673^{+12}_{-14}	$38.5^{+5.6}_{-5.8}$	$41.1^{+6.2}_{-8.0}$	$41.8^{+1.3}_{-1.1}$	$44.8^{+8.1}_{-7.5}$	5.89 ± 0.51
	3	5590^{+24}_{-93}	2906^{+20}_{-22}	4216^{+21}_{-19}	1470^{+15}_{-17}	$57.1^{+10.7}_{-9.5}$	$48.5^{+17.0}_{-20.4}$	$32.6^{+16.1}_{-18.2}$	$34.9^{+59.4}_{-16.6}$	6.17 ± 0.13
	4	5783^{+97}_{-34}	2984^{+28}_{-22}	6181^{+46}_{-28}	1861^{+35}_{-32}	$46.9^{+6.0}_{-11.2}$	$48.9^{+5.5}_{-18.0}$	$29.4^{+10.0}_{-4.0}$	$48.2^{+12.4}_{-18.1}$	5.78 ± 0.31
PG 1001+054	All	1688^{+21}_{-21}	1325^{+18}_{-18}	1933^{+31}_{-20}	1370^{+44}_{-62}	$99.4^{+15.8}_{-27.2}$	$68.0^{+11.2}_{-16.0}$	$65.5^{+5.6}_{-3.9}$	$63.3^{+17.4}_{-11.2}$	4.46 ± 0.35
	3	1666^{+11}_{-11}	1318^{+11}_{-11}	917^{+60}_{-50}	840^{+134}_{-185}	$57.6^{+18.9}_{-13.5}$	$63.0^{+22.6}_{-28.1}$	$64.7^{+11.2}_{-6.9}$	$117.0^{+11.5}_{-62.5}$	4.93 ± 0.22
PG 1048+342	All	2905^{+27}_{-59}	1797^{+16}_{-16}	2147^{+8}_{-7}	1175^{+16}_{-14}	$24.8^{+10.4}_{-8.7}$	$32.6^{+13.3}_{-32.6}$	$36.8^{+2.4}_{-3.4}$	$31.8^{+77.2}_{-35.5}$	3.52 ± 0.41
	1	3004^{+34}_{-45}	1840^{+16}_{-14}	3043^{+33}_{-34}	1449^{+36}_{-31}	$26.2^{+8.6}_{-8.2}$	$25.5^{+13.7}_{-8.2}$	$28.0^{+5.6}_{-4.8}$	$33.6^{+11.1}_{-11.9}$	3.02 ± 0.21
PG 1100+772	All	5733^{+32}_{-21}	3449^{+31}_{-30}	11229^{+29}_{-23}	4002^{+87}_{-110}	$44.9^{+30.5}_{-30.8}$	$37.4^{+45.3}_{-27.5}$	$55.9^{+3.0}_{-1.4}$	$48.6^{+46.6}_{-120.9}$	41.95 ± 3.85
PG 1202+281	All	5199^{+24}_{-22}	2035^{+5}_{-4}	4255^{+23}_{-17}	1301^{+18}_{-24}	$98.5^{+28.2}_{-30.1}$	$66.4^{+65.7}_{-13.4}$	$66.3^{+2.3}_{-1.9}$	$116.3^{+39.4}_{-31.4}$	3.42 ± 0.32
	1	4891^{+19}_{-19}	3412^{+12}_{-12}	3825^{+38}_{-70}	1597^{+17}_{-19}	$50.0^{+6.6}_{-4.6}$	$50.4^{+7.9}_{-5.1}$	$48.7^{+3.5}_{-3.9}$	$74.4^{+8.8}_{-27.8}$	3.52 ± 0.24
	3	4863^{+22}_{-16}	3260^{+20}_{-17}	3814^{+399}_{-747}	1540^{+53}_{-63}	$71.6^{+15.6}_{-9.5}$	$68.7^{+36.6}_{-7.1}$	$69.5^{+4.8}_{-4.4}$	$133.0^{+28.2}_{-68.8}$	3.45 ± 0.36
	4	4949^{+16}_{-16}	3738^{+25}_{-24}	3658^{+26}_{-29}	1428^{+29}_{-33}	$53.3^{+10.9}_{-8.5}$	$46.5^{+22.4}_{-11.1}$	$63.3^{+13.3}_{-12.9}$	$79.4^{+37.4}_{-22.1}$	3.22 ± 0.21
PG 1211+143	All	1918^{+95}_{-95}	1499^{+49}_{-49}	1358^{+14}_{-11}	697^{+18}_{-19}	$33.0^{+5.6}_{-5.5}$	$47.5^{+10.8}_{-8.9}$	$53.0^{+5.1}_{-5.8}$	$43.7^{+18.2}_{-17.5}$	4.94 ± 0.56
PG 1310-108	All	3613^{+812}_{-781}	1978^{+87}_{-65}	2425^{+15}_{-19}	1092^{+36}_{-54}	$13.2^{+3.8}_{-2.8}$	$12.5^{+3.6}_{-2.1}$	$12.8^{+1.7}_{-1.7}$	$12.6^{+6.8}_{-3.5}$	0.33 ± 0.01
PG 1351+640	All	7625^{+95}_{-81}	3114^{+65}_{-50}	2154^{+18}_{-13}	1527^{+23}_{-21}	$68.6^{+20.4}_{-20.7}$	$61.6^{+81.3}_{-27.6}$	$74.8^{+2.3}_{-2.3}$	$-31.5^{+77.8}_{-37.2}$	4.87 ± 0.69
PG 1351+695	All	5297^{+10}_{-10}	1871^{+6}_{-6}	4478^{+3}_{-3}	1583^{+12}_{-10}	$18.6^{+2.3}_{-2.0}$	$16.7^{+4.1}_{-1.9}$	$19.9^{+1.0}_{-1.0}$	$11.7^{+6.0}_{-5.3}$	0.50 ± 0.06
PG 1501+106	All	5006^{+50}_{-32}	2490^{+47}_{-47}	4152^{+8}_{-5}	1986^{+14}_{-17}	$26.0^{+2.0}_{-2.2}$	$24.0^{+4.6}_{-6.1}$	$22.0^{+0.5}_{-0.4}$	$113.7^{+10.7}_{-66.2}$	1.03 ± 0.14
	1	5081^{+26}_{-44}	2528^{+50}_{-43}	3855^{+13}_{-14}	2291^{+18}_{-19}	$24.1^{+10.8}_{-8.8}$	$6.1^{+17.9}_{-3.2}$	$5.0^{+1.3}_{-1.4}$	$117.0^{+7.5}_{-43.7}$	1.20 ± 0.11
	3	5002^{+34}_{-53}	2454^{+47}_{-44}	4141^{+5}_{-5}	1384^{+10}_{-12}	$24.8^{+1.6}_{-1.4}$	$24.9^{+1.8}_{-1.6}$	$42.9^{+9.9}_{-4.7}$	$25.9^{+3.0}_{-1.8}$	1.03 ± 0.09
	4	4718^{+43}_{-41}	2378^{+56}_{-45}	2945^{+17}_{-18}	1156^{+14}_{-14}	$32.2^{+3.6}_{-4.0}$	$24.8^{+16.8}_{-7.5}$	$43.7^{+3.7}_{-2.7}$	$108.8^{+5.5}_{-23.0}$	0.86 ± 0.06
PG 1534+580	All	4217^{+751}_{-155}	3180^{+84}_{-47}	2362^{+11}_{-7}	1142^{+20}_{-20}	$26.0^{+5.7}_{-8.6}$	$35.5^{+3.5}_{-21.6}$	$25.4^{+2.0}_{-1.4}$	$28.2^{+9.3}_{-14.0}$	0.48 ± 0.03
PG 1613+658	All	$10{,}269^{+773}_{-167}$	3927^{+13}_{-16}	6762^{+9}_{-10}	3504^{+13}_{-14}	$51.2^{+5.2}_{-6.0}$	$55.8^{+10.5}_{-22.9}$	$52.4^{+3.4}_{-2.8}$	$27.6^{+13.0}_{-13.0}$	8.62 ± 1.04
	1	9866^{+118}_{-132}	3907^{+14}_{-13}	12817^{+36}_{-30}	4654^{+18}_{-16}	$49.7^{+9.2}_{-10.2}$	$42.9^{+31.1}_{-10.9}$	$79.3^{+5.9}_{-2.8}$	$91.8^{+10.0}_{-32.7}$	9.36 ± 1.16
	2	$10{,}998^{+193}_{-221}$	3926^{+13}_{-14}	11469^{+25}_{-48}	4196^{+20}_{-29}	$46.3^{+7.3}_{-7.3}$	$45.9^{+11.4}_{-13.3}$	$48.3^{+5.0}_{-3.8}$	$-191.1^{+223.2}_{-11.0}$	8.34 ± 0.85

Note. The line widths of the rms spectra of PG 0049+171, PG 0947+396, PG 1202+281, PG 1351+640, and PG 1501+106 are measured from their continuum-cleaned rms spectra (See Section 3.1). The broadening caused by the instrument and seeing has been corrected. For 5100 Å luminosity, the galactic extinction (Schlafly & Finkbeiner 2011) is corrected, but the host-galaxy contamination is not removed. The time lags in the table are in the rest frame.

light curves can perhaps differ. BLR dynamical modeling (e.g., Pancoast et al. 2011, 2014; Li et al. 2013, 2018) can, in principle, give more reliable BH mass measurements if the BLRs deviate from Keplerian/virialized motion, but this discussion stretches beyond the scope of the current paper. The best data sets here may be good enough to allow dynamical modeling, which we shall investigate in future work.

For each object, we list the measurements from the whole light curve and from all of the seasons (except for the very poor ones) in Table 7 and mark the preferred values with a "✓" (the ones calculated from $\sigma_{\rm H\beta}$ in the rms spectra). We prefer to adopt the results with the smallest measurement uncertainties. They are usually the values measured from the whole light curves, except for those objects for which the lag measurements of individual seasons have comparable or significantly smaller measurement uncertainties.

3.7. Velocity-resolved Results

To investigate the BLR geometry and kinematics and their potential changes over time for the present sample, we calculated velocity-resolved lags (e.g., Bentz et al. 2009; Denney et al. 2010; Grier et al. 2013; Du et al. 2016a; Hu et al. 2020a) as a first step. We divided the emission lines into several bins, determined by the flux ranges in the rms spectra, and measured their time lags with respect to the continuum using ICCF. The lags as functions of velocity are shown in Figure 18. Similar to the BH mass measurements in Section 3.6, because of the limitations of variation amplitudes

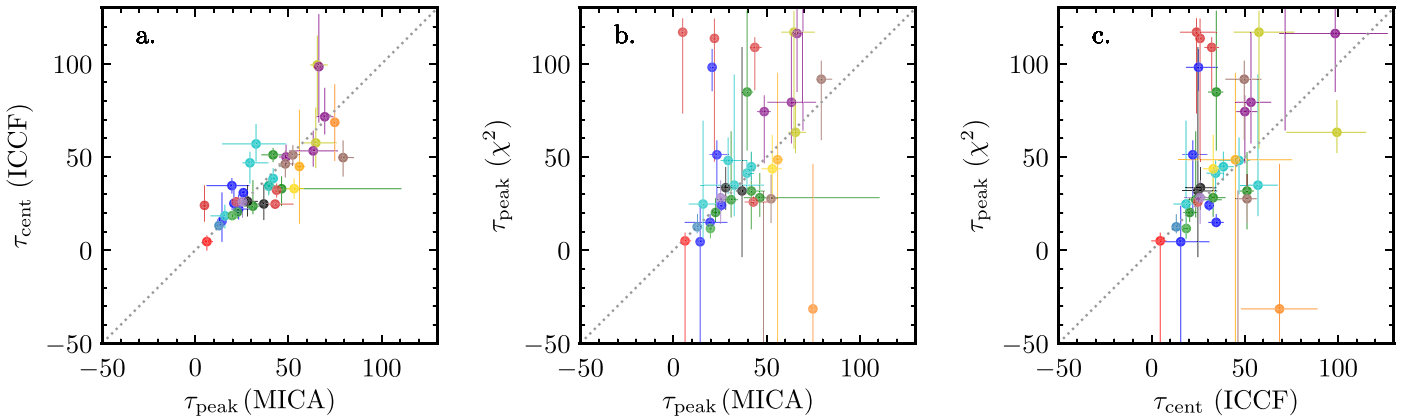

Figure 17. Pairwise correlations between the measurements from ICCF, χ^2, and MICA. The points in the same color are the time lags of different seasons (and the entire light curve) for individual objects.

and S/N ratios, we cannot obtain the velocity-resolved lag measurements for all of the objects for all individual seasons. We did not calculate the velocity-resolved lags for the seasons with poor data or no clear variations. For the objects with very weak Hβ signals in the rms spectra (see Section 3.1), we instead determined their velocity bins using the mean spectra. It has been demonstrated that using mean or rms spectra to determine the velocity bins does not usually change the results significantly (see more details in Paper I).

4. Discussion

One of the primary goals of the MAHA project is to investigate the BLR geometry and kinematics as well as their potential evolution in AGN BLRs with asymmetric Hβ lines, which requires both long-term monitoring and high cadence. More than half of the present sample (nine objects) have been monitored for 4–5 yr with cadences of ∼3–8 days. Among them, six objects (see Table 7) show clear variations in more than one season and can be used to investigate the potential evolution in their BLR responses. Here we discuss the measurements of the individual objects and compare them with the previous results in the literature.

4.1. Notes for Individual Objects

PG 0007+106 (Mrk 1501, III Zw 2): It is a radio-loud AGN and showed a 5.1 yr quasiperiodicity in its radio light curve, which can perhaps be explained by the helical motion of a jet (Teräsranta et al. 2005; Li et al. 2010). In our RM campaign, Hβ time lags of ∼14–25 days (MICA) were measured for different seasons. From the four seasons and the combined light curve, BH mass measurements of 4–7 $\times$ $10^7 M_\odot$ were obtained using the line dispersion for the velocity measurement ($7.03^{+0.34}_{-0.31}$ $\times$ $10^7 M_\odot$ is preferred). The previous RM campaign of this object (Grier et al. 2012) gave a time lag of $15.5^{+2.2}_{-1.8}$ days and a BH mass of $\log(M_\bullet/M_\odot) = 7.9^{+0.2}_{-0.2}$ was measured from BLR dynamical modeling (Grier et al. 2017). Our BH mass is in excellent agreement with that from Grier et al. (2017). In all of the four seasons, the velocity-resolved lags in Figure 18 show longer lags at small velocities and shorter lags at high velocities, which indicates that its BLR is dominated by virialized motions or a Keplerian disk (the data quality in Seasons 1 and 4 is relatively poorer). In Seasons 2 and 3, the velocities corresponding to the blue wing of the line have slightly longer lags than the red wing, implying a potential contribution of inflowing velocity besides the Keplerian/virialized motion in its BLR. Similarly, the BLR modeling in Grier et al. (2017) suggested that its BLR kinematics is a combination of near-circular elliptical and inflowing orbits. However, the velocity-resolved lags in Grier et al. (2013) showed a stronger inflowing signature. In our campaign, the Hβ profile is almost the same as that in Grier et al. (2012) and also similar to those seen in much earlier single-epoch spectra (De Robertis 1985; Boroson & Green 1992; Marziani et al. 2003a). Note that the excess red emission in the Hβ profile for this object is not well characterized by the De Robertis asymmetry parameter A. The A parameter measures the blue or red extension of line wing. The red wing of the Hβ in PG 0007+106 does not extend too much with respect to its line core. Instead the flux excess can be quantified by a systematic velocity shift (e.g., "Hβ shift" in Table 2 of Boroson & Green 1992). The relation between the BLR kinematics and emission-line profiles (including the velocity shift) will be discussed in detail in a forthcoming paper.

PG 0049+171 (Mrk 1148): The profile of its broad Hβ is slightly red asymmetric and showed no significant change during our campaign. Its profile remains similar to that in De Robertis (1985) and Boroson & Green (1992). The Hβ response in Season 4 is the best among the seasons. It gives a BH mass of $2.95^{+0.37}_{-0.31}$ $\times$ $10^7 M_\odot$. Considering that the line signal in the rms spectrum of Season 4 is not very significant (it is better in the continuum-cleaned rms spectrum), we prefer to use the mean spectrum to determine the velocity bins in the velocity-resolved analysis. In the velocity-resolved analysis, the plateau of the Hβ light curve at the end of Season 1 is too short to give a good constraint in some of the velocity bins; thus the lags at different velocities in Season 1 are not very well resolved. The velocity-resolved lags for the other seasons (Seasons 2, 3, 4) are almost the same and show longer lags in low-velocity bins and shorter lags at high velocities. Similar to PG 0007+106, which is the signature of a Keplerian disk or virialized motion. Moreover, compared to Season 3, the velocity-resolved lags in Seasons 2 and 4 look more symmetric. The lags for the blue wing for Seasons 3 are shorter than those for its red wing, which indicates a potential contribution from outflow in this season. The differences between Seasons 2, 3, and 4 may imply that the response region of the BLR in PG 0049+171 is undergoing some minor changes.

Table 7
Virial Products and Masses of the Black Holes

Target	Season	VP (Mean)	BH mass (rms)		Note
		$R_{\rm H\beta}V^2_{\rm FWHM}/G$	$1.12 \times R_{\rm H\beta}V^2_{\rm FWHM}/G$	$4.47 \times R_{\rm H\beta}\sigma^2_{\rm line}/G$	
	($\times 10^7 M_\odot$)	($\times 10^7 M_\odot$)	($\times 10^7 M_\odot$)		
PG 0007+106	All	$14.16^{+0.68}_{-0.62}$	$13.18^{+0.61}_{-0.56}$	$7.03^{+0.34}_{-0.31}$	✓
	1	$13.10^{+3.50}_{-2.23}$	$14.84^{+3.97}_{-2.53}$	$7.31^{+1.96}_{-1.26}$	
	2	$10.56^{+5.02}_{-7.33}$	$9.18^{+4.37}_{-6.38}$	$6.07^{+2.89}_{-4.22}$	
	3	$8.27^{+1.45}_{-1.52}$	$6.27^{+1.10}_{-1.15}$	$3.84^{+0.68}_{-0.71}$	
	4	$10.86^{+1.11}_{-1.03}$	$9.97^{+1.01}_{-0.94}$	$4.40^{+0.45}_{-0.42}$	
PG 0049+171	All	$14.02^{+2.95}_{-0.94}$	$7.13^{+0.60}_{-0.46}$	$4.91^{+0.42}_{-0.34}$	
	1	$13.92^{+3.58}_{-2.13}$	$7.18^{+1.24}_{-1.09}$	$4.49^{+0.79}_{-0.70}$	
	2	$11.83^{+2.55}_{-2.94}$	$5.77^{+0.68}_{-1.41}$	$5.07^{+0.61}_{-1.25}$	
	3	$16.69^{+23.30}_{-3.11}$	$3.64^{+5.06}_{-0.67}$	$3.95^{+5.49}_{-0.75}$	
	4	$7.85^{+2.02}_{-0.78}$	$5.79^{+0.70}_{-0.57}$	$2.95^{+0.37}_{-0.31}$	✓
PG 0923+129	All	$0.74^{+0.38}_{-0.21}$	$0.62^{+0.32}_{-0.18}$	$0.81^{+0.42}_{-0.23}$	✓
PG 0947+396	All	$22.79^{+2.19}_{-1.18}$	$9.35^{+0.91}_{-0.45}$	$14.06^{+1.40}_{-0.76}$	
	1	$8.47^{+3.72}_{-4.13}$	$4.91^{+2.16}_{-2.40}$	$3.80^{+1.67}_{-1.86}$	
	2	$21.70^{+0.90}_{-0.63}$	$22.87^{+0.74}_{-0.65}$	$10.22^{+0.36}_{-0.33}$	✓
	3	$19.90^{+9.79}_{-11.13}$	$12.68^{+6.24}_{-7.08}$	$6.16^{+3.03}_{-3.44}$	
	4	$19.16^{+6.53}_{-2.64}$	$24.52^{+8.33}_{-3.37}$	$8.87^{+3.03}_{-1.26}$	
PG 1001+054	All	$3.65^{+0.32}_{-0.23}$	$5.35^{+0.49}_{-0.34}$	$10.73^{+1.15}_{-1.17}$	✓
	3	$3.50^{+0.61}_{-0.38}$	$1.19^{+0.26}_{-0.18}$	$3.99^{+1.45}_{-1.81}$	
PG 1048+342	All	$6.07^{+0.41}_{-0.61}$	$3.71^{+0.24}_{-0.34}$	$4.44^{+0.31}_{-0.42}$	✓
	1	$4.94^{+0.99}_{-0.86}$	$5.68^{+1.14}_{-0.98}$	$5.14^{+1.06}_{-0.90}$	
PG 1100+772	All	$35.86^{+1.99}_{-0.91}$	$154.05^{+8.39}_{-3.78}$	$78.13^{+5.44}_{-4.72}$	✓
PG 1202+281	All	$34.99^{+1.27}_{-1.02}$	$26.25^{+0.96}_{-0.76}$	$9.80^{+0.44}_{-0.46}$	✓
	1	$22.76^{+1.66}_{-1.81}$	$15.59^{+1.17}_{-1.36}$	$10.85^{+0.82}_{-0.90}$	
	3	$32.08^{+2.21}_{-2.05}$	$22.10^{+4.87}_{-8.77}$	$14.39^{+1.40}_{-1.50}$	
	4	$30.26^{+6.35}_{-6.18}$	$18.51^{+3.89}_{-3.79}$	$11.26^{+2.41}_{-2.36}$	
PG 1211+143	All	$3.81^{+0.53}_{-0.56}$	$2.14^{+0.21}_{-0.24}$	$2.25^{+0.25}_{-0.28}$	✓
PG 1310-108	All	$3.25^{+1.53}_{-1.47}$	$1.64^{+0.22}_{-0.22}$	$1.33^{+0.20}_{-0.22}$	✓
PG 1351+640	All	$84.95^{+3.38}_{-3.18}$	$7.60^{+0.27}_{-0.25}$	$15.24^{+0.66}_{-0.64}$	✓
PG 1351+695	All	$10.88^{+0.57}_{-0.55}$	$8.71^{+0.46}_{-0.44}$	$4.35^{+0.24}_{-0.23}$	✓
PG 1501+106	All	$10.76^{+0.32}_{-0.25}$	$8.29^{+0.19}_{-0.16}$	$7.57^{+0.20}_{-0.20}$	
	1	$2.51^{+0.66}_{-0.73}$	$1.61^{+0.42}_{-0.47}$	$2.28^{+0.60}_{-0.66}$	
	3	$20.95^{+4.84}_{-2.33}$	$16.08^{+3.71}_{-1.76}$	$7.17^{+1.66}_{-0.79}$	✓
	4	$18.97^{+1.65}_{-1.22}$	$8.28^{+0.71}_{-0.52}$	$5.09^{+0.45}_{-0.34}$	
PG 1534+580	All	$8.80^{+3.21}_{-0.82}$	$3.09^{+0.24}_{-0.18}$	$2.89^{+0.25}_{-0.19}$	✓
PG 1613+658	All	$107.82^{+17.70}_{-6.74}$	$52.36^{+3.42}_{-2.79}$	$56.13^{+3.69}_{-3.02}$	✓
	1	$150.70^{+11.72}_{-6.63}$	$284.85^{+21.14}_{-10.01}$	$149.95^{+11.16}_{-5.32}$	
	2	$114.07^{+12.36}_{-10.16}$	$138.95^{+14.25}_{-11.11}$	$74.24^{+7.64}_{-5.99}$	

Note. The VP are calculated from the FWHM of mean spectra. BH masses are estimated using the FWHM and the sigma of rms spectra. The propagation errors are from line widths and time lags, and the uncertainties of f factor is not considered here. The last column notes the data set we preferred for the BH mass measurement.

PG 0923+129 (Mrk 705, Ark 202): We have only data of one season for this object and they varied strongly only toward the end of our campaign. An Hβ time lag is reported here for the first time. The time lag measured from MICA is $6.2^{+3.2}_{-1.8}$ days and the corresponding preferred BH mass is $0.81^{+0.42}_{-0.23} \times 10^7 M_\odot$. The broad H$\beta$ profile is slightly red asymmetric, and neither the Fe II or [O III] lines are particularly strong. Its velocity-resolved lags are clearly longer at blue velocities and shorter at red velocities, which is the signature of inflow (see Figure 18).

PG 0947+396: Its Hβ profile shows a red asymmetry and has no obvious changes compared with previous spectra published by Boroson & Green (1992) and Shang et al. (2007). Time lags can be detected for each of its four seasons, although the uncertainties for the second season are the smallest because of its stronger continuum variation and clear Hβ response (See Section 3.1). The MICA measurement from the entire light curve is consistent with the single-season result from Season 2 ($39.5^{+3.8}_{-1.7}$ days versus $41.8^{+1.3}_{-1.1}$ days). The lag in Season 2 yields a preferred BH mass of $1.02^{+0.04}_{-0.03} \times 10^8 M_\odot$. Its velocity-resolved lags in Seasons 1, 3, and 4 are generally symmetric with longer lags at small velocities and shorter lags at high velocities, which is the signature of a Keplerian disk or virialized motion (similar to PG 0007+106 and PG 0049 +171). The lags at blue velocities are a little longer than those at red velocities in Seasons 1 and 3, while the opposite is the case in Season 4. While this effect is not very pronounced, it may imply weak contributions from inflow and outflow, respectively. It is a little strange that the lags at different velocities in Season 2 are not fully resolved, although the

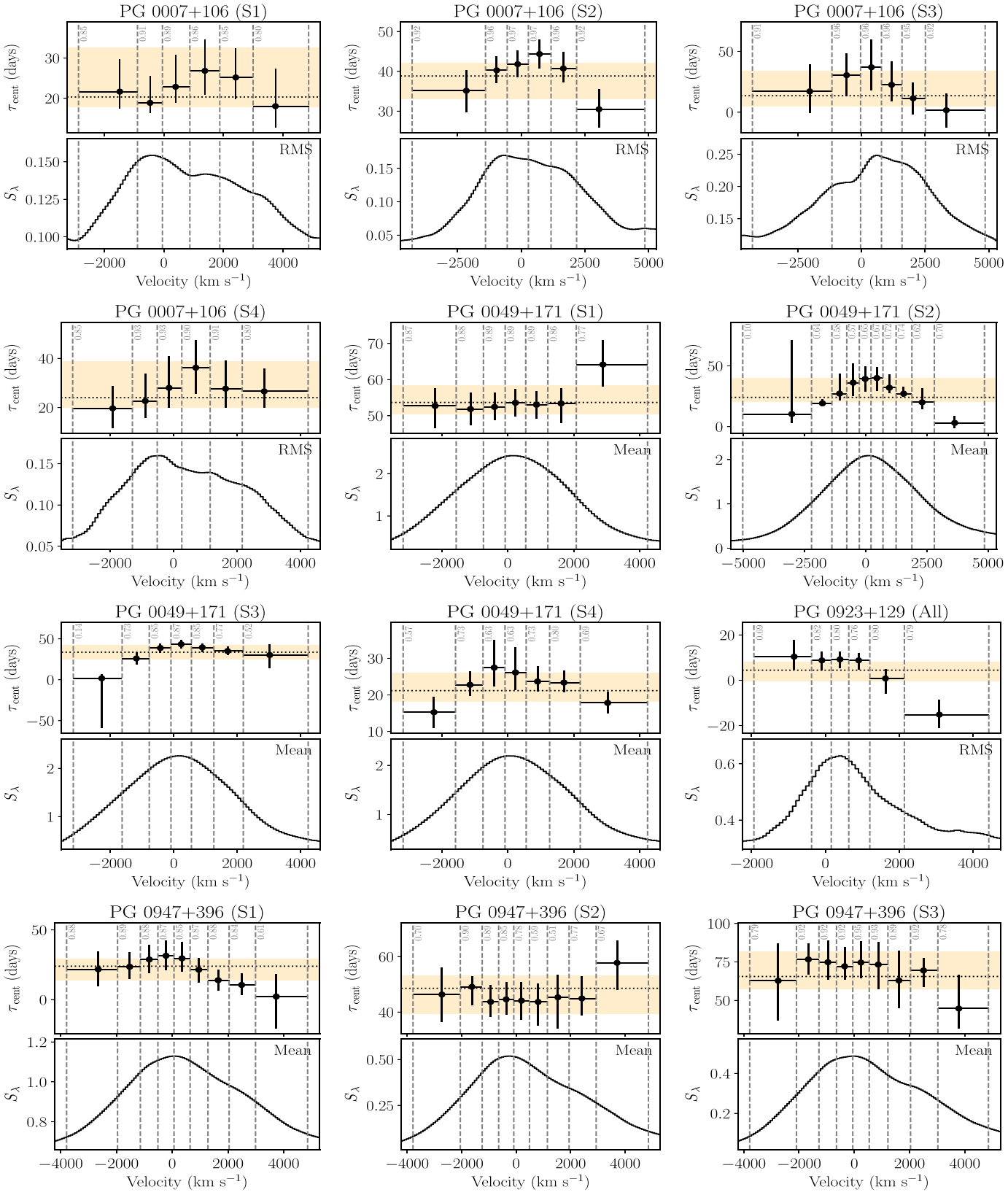

Figure 18. Velocity-resolved lags. The upper subpanel in each panel is the velocity-resolved lags, and the lower subpanel is the rms or mean spectrum. The horizontal dash lines and yellow horizontal spans are the mean time lags and their uncertainties. The vertical dashed lines mark the edges of the velocity bins. The peak correlation coefficient is denoted in each bin at the top subpanels.

uncertainties of the average lag measurement is the smallest of the four seasons, which may result from its relatively small variation amplitude of the light curves in this season.

PG 1001+054: The Hβ profile shows significant blue asymmetry (see Table 1 and Figure 6). It has stronger Fe II emission lines (see Figure 1) compared to the other objects,

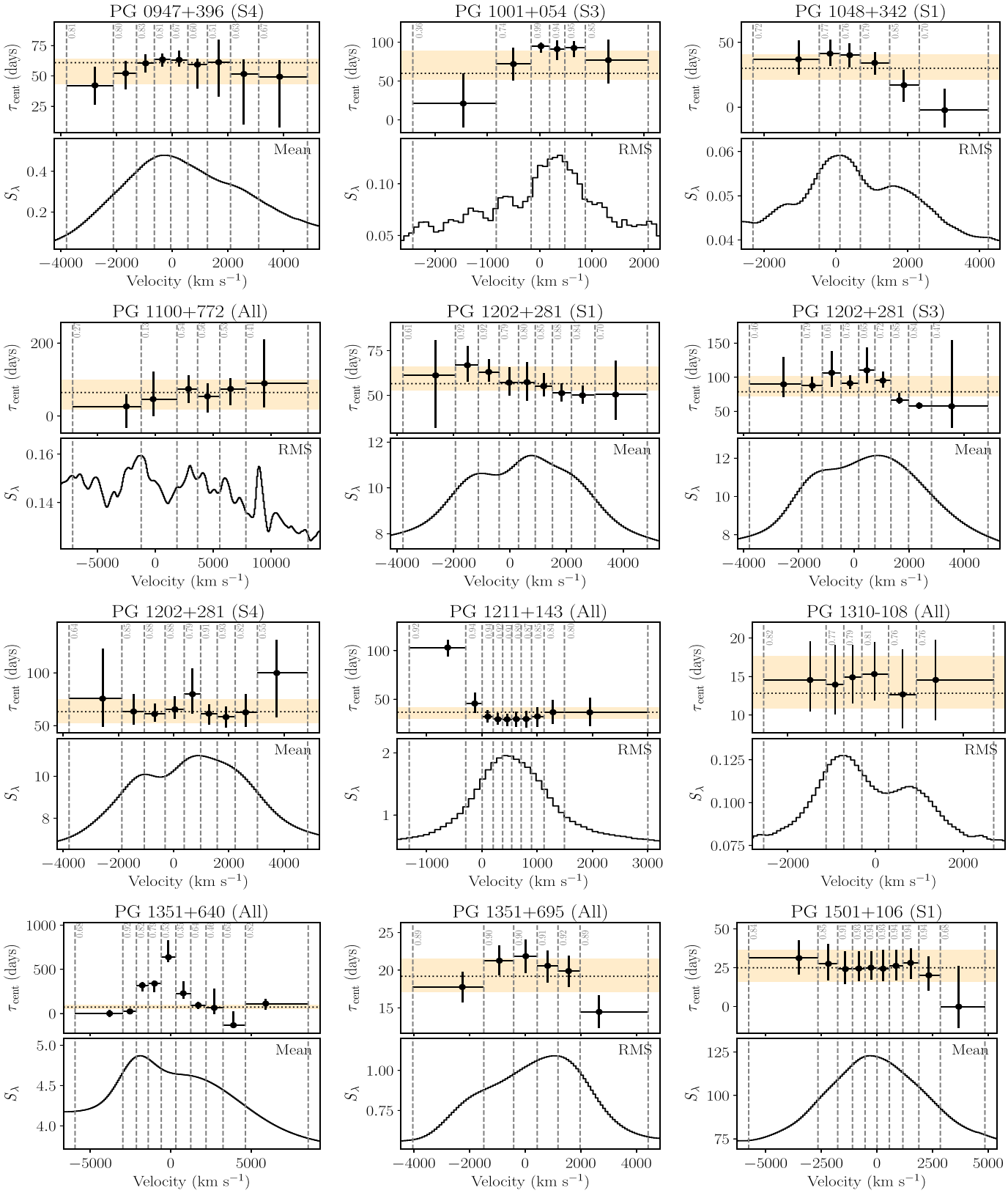

Figure 18. (Continued.)

which is consistent with the positive correlation between the asymmetry parameter A and the relative strength of Fe II reported by Boroson & Green (1992). We prefer the BH mass measured from the entire combined light curve. The BH mass measured in our campaign is $1.07^{+0.12}_{-0.12} \times 10^8 M_\odot$. Its velocity-resolved lag measurement in Season 3 suggests an outflow signature (shorter lags at blue velocities and longer at red).

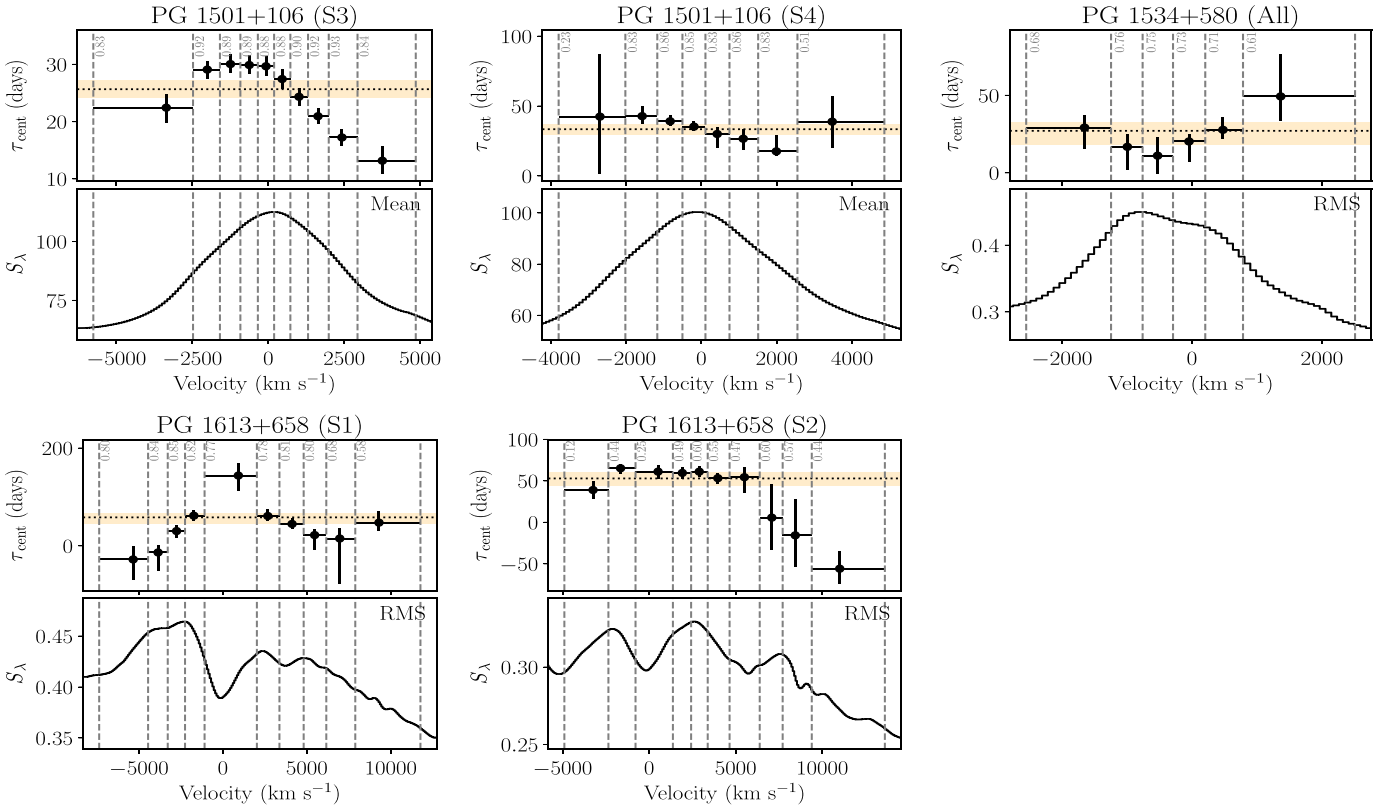

Figure 18. (Continued.)

PG 1048+342: The profile of its broad Hβ shows a more significant red asymmetry compared to the profiles in Boroson & Green (1992) and Kaspi et al. (2000), but it displayed no significant changes over the four seasons in our campaign. Kaspi et al. (2000) did not manage to sample this object sufficiently to successfully measure the time lag of its Hβ line. The clear variation (especially in Season 1 and in the entire light curve) enables us to give a reliable measurement of its Hβ time lag for the first time. The time lag measured from the entire light curve ($36.8^{+2.4}_{-3.4}$ days) using MICA has smaller uncertainties than that from Season 1 ($28.0^{+5.6}_{-4.8}$ days) and is thus preferred for the BH mass determination, which we calculate to be $4.44^{+0.31}_{-0.42} \times 10^7 M_\odot$. The longer lags at blue velocities and shorter lags at red velocities measured from Season 1 show the signature of inflow.

PG 1100+772 (3C 249.1): Although the variability of Hβ ($F_{\rm var} = 1.6\%$) is much smaller than that of the 5100 Å continuum flux ($F_{\rm var} = 8.9\%$, see Table 3), we can still measure a Hβ time lag using MICA. The ICCF and χ^2 methods cannot give reliable measurements to the lags because of the small line variation amplitude. The profile of its broad Hβ shows clear red asymmetry. The time lag measured from the entire light curve is $55.9^{+3.0}_{-1.4}$ days and the BH mass is $7.81^{+0.54}_{-0.47} \times 10^8 M_\odot$. It is a radio-loud object (Fanaroff–Riley II) with asymmetric radio lobes and has an extended emission-line region. Its jets and its extended emission-line region were suggested to originate from the merger of the host galaxy of a gas-poor quasar and a large late-type galaxy (Stockton & Mackenty 1983; Gilbert et al. 2004; Fu & Stockton 2009). Because of the small variation of Hβ flux, the profile of the rms spectrum is poorly constrained. The lags at different velocities are only marginally resolved. On average, the lags at blue velocities are shorter than those in the red, which may indicate an outflow (not on a significant scale because of the small variation amplitude).

PG 1202+281 (GQ Com): The Hβ time lag is reported here for the first time. The profile of its broad Hβ shows a red asymmetry. The peak of Hβ was blueshifted in previous spectra from Boroson et al. (1985), Boroson & Green (1992), Kaspi et al. (2000), and Shang et al. (2007); however such a blueshift does not seem so evident during our campaign. The light curves in Seasons 1 and 3 (and the entire light curve) show clear variations and can give reliable lag measurements. However, the lag measured from the entire light curve has the smallest uncertainties and is preferred for the BH mass determination. This yields a BH mass of $9.80^{+0.44}_{-0.46} \times 10^7 M_\odot$. Similar to PG 0049+171, we use the line profiles in the mean spectra to determine the velocity bins in the velocity-resolved analysis because of the relatively poor quality of the rms spectra. Its velocity-resolved lags generally show the signature of inflow (see Seasons 1 and 3; the lags at blue velocities are longer than the red ones).

PG 1211+143: The X-ray and UV observations suggest that this object has ultrafast outflows (Pounds et al. 2003; Danehkar et al. 2017). It is therefore interesting to investigate the kinematics of its BLR through RM. As a narrow-line Seyfert 1 galaxy, this object was monitored from 1991 to 1998 by Kaspi et al. (2000) and showed a Hβ time lag of $93.2^{+19.7}_{-29.9}$ days (Kaspi et al. 2005). Because the variation of its light curve in the previous campaign (Kaspi et al. 2000) was slow and the cadence was also not very high, the past result has relatively

Table 8
Hβ Asymmetry vs. BLR Kinematics

Target	$R_{\rm Fe}$	Hβ Asymmetry	BLR Kinematics
PG 0007+106	0.48	Symmetric	Keplerian/Virialized + weak inflow
PG 0049+171	0.13	Red	Keplerian/Virialized + weak outflow
PG 0923+129	0.53	Red	Inflow
PG 0947+396	0.33	Red	Keplerian/Virialized + weak inflow/outflow
PG 1001+054	0.89	Blue	Outflow
PG 1048+342	0.28	Red	Inflow
PG 1100+772	0.05	Red	Outflow
PG 1202+281	0.19	Red	Inflow
PG 1211+143	0.51	Blue	Inflow
PG 1310-108	0.23	Red	Unresolved
PG 1351+640	0.20	Red	Keplerian/Virialized
PG 1351+695	0.47	Symmetric	Keplerian/Virialized + inflow
PG 1501+106	0.26	Red	Inflow
PG 1534+580	0.21	Red	Complicated
PG 1613+658	0.57	Red	Inflow

Note. $R_{\rm Fe}$ is the flux ratio of Fe II and Hβ emission lines measured from our campaign (from an individual exposure with a high S/N ratio).

large uncertainties. Given the higher cadence in our campaign (∼4 days), the time lag becomes better defined, and we find it to be significantly shorter ($53.0^{+5.1}_{-5.8}$ days). The BH mass of $\log(M_\bullet/M_\odot) = 7.87^{+0.19}_{-0.19}$ given in Peterson et al. (2004) is larger than the value reported here ($2.14^{+0.21}_{-0.24} \times 10^7 M_\odot$ or $2.25^{+0.25}_{-0.28} \times 10^7 M_\odot$ from the FWHM or $\sigma_{\rm line}$ of the rms spectrum). The longer lags at blue velocities and the shorter at red (see Figure 18) suggest an inflowing BLR. This is the first determination of the BLR kinematics in this object.

PG1310−108: The Hβ time lag is reported here for the first time. This object historically showed an Hβ profile with a strong and extended red wing (Boroson & Green 1992). The Hβ light curve shows clear response to the varying continuum with a time lag of $12.8^{+1.7}_{-1.7}$ days. The BH mass measured from our campaign is $1.33^{+0.20}_{-0.22} \times 10^7 M_\odot$. Its lags at different velocities are not successfully resolved.

PG 1351+640: Kaspi et al. (2000) monitored this object in 1991–1998 but did not find a reliable Hβ lag measurement because of the relatively low cadence and large scatter of points in the light curve. Our data demonstrate significant variations and clear responses. The ICCF and MICA results are consistent with each other. The rms spectrum shows some residual signal around the [O III] wavelengths, which may originate from the variations in the contribution of the broad He Iλ4922,5016 lines (e.g., Jackson & Browne 1989) or a broad component of [O III] (e.g., Zakamska et al. 2016). The Fe II lines in this object are weak (see Table 8), so this residual signal is less likely from Fe IIλ4924,5018 lines. Because of the long-term variation timescale, we did not separate the light curves into different seasons. The time lag measured from the entire light curves in our campaign is $74.8^{+2.3}_{-2.3}$ days, and the BH mass is $1.52^{+0.07}_{-0.06} \times 10^8 M_\odot$. Similar to PG 0049+171, we used the line profile in the mean spectrum to determine the bins of velocity-resolved analysis because of the relatively lower S/N ratio of the rms spectrum. The inferred BLR kinematics is Keplerian/virialized motion.

PG 1351+695 (Mrk 279): Its Hβ variation amplitude in the present campaign is around $F_{\rm var} = 27\%$, which is stronger than the continuum variability ($F_{\rm var} = 12\%$), probably because the continuum flux is diluted by the contribution from its host galaxy. This object was first monitored from 1987 December to 1988 July with 39 points by Maoz et al. (1990), who reported a Hβ time lag of 12 ± 3 days. After that, it was monitored again from 1996 January to 1996 July by Santos-Lleó et al. (2001), giving a lag of $16.7^{+5.3}_{-5.6}$ days. More recently, Barth et al. (2015) reported a new RM measurement for this object from 2011 March to 2011 June, with a time lag consistent with the previous measurements (see also Williams et al. 2018). The time lag in the present paper is $19.9^{+1.0}_{-1.0}$ days, and the derived BH mass is $4.35^{+0.24}_{-0.23} \times 10^7 M_\odot$. Its velocity-resolved lags show a Keplerian disk or virialized motion of the BLR with probable contributions from inflow (see Figure 18).

PG 1501+106 (Mrk 841): We monitored this object for 4 yr (from 2017 to 2020). The light curve of the first season was published in Paper II. In the present paper, we slightly adjusted the window for measuring the Hβ fluxes in order to make sure that the variation signals in the rms spectra of all four seasons are covered. We used PyCALI (Li et al. 2014) to perform the intercalibration of the spectroscopic and photometric continuum light curves, which is different from the simple linear regression method in Paper II. This also makes the time lag measured from Season 1 slightly different but within 1σ uncertainties with respect to the value provided in Paper II. The variation of Season 2 is too weak to give a good constraint to the time lag; however Seasons 3 and 4 show clear and strong Hβ responses. It should be noted that the peak around JD ∼2458700 days in the Hβ light curve in Season 3 and the trough around JD ∼2459000 days in Season 4 are both narrower than their corresponding features in the continuum light curve (see Figure 14). This phenomenon makes the transfer function calculated through MICA for Seasons 3 and 4 have a second very broad component in addition to the primary narrow peak (see Figure 14). Although Season 3 has a very broad component in the transfer function from MICA, we still prefer to use the lag from this season in the BH mass measurement because its variability is the strongest during the campaign. The three methods (ICCF, χ^2, and MICA) yield generally consistent time lags for Season 3. The preferred BH mass measurement is $7.17^{+1.66}_{-0.79} \times 10^7 M_\odot$, which is slightly larger than the measurement in Paper II. U et al. (2022) monitored this object one year before our campaign although their light curves are of shorter duration. They obtained a BH mass measurement ($4.7^{+2.6}_{-1.6} \times 10^7 M_\odot$) slightly smaller than

ours in the present paper (but within 1σuncertainties). The velocity-resolved lags in Season 1 are not clear, as reported in Paper II, but both of the velocity-resolved lags in Seasons 3 and 4 show definite inflow signatures. This is consistent with the BLR kinematics reported by U et al. (2022).

PG 1534+580 (Mrk 290): This object was monitored before by Denney et al. (2010) who reported a time lag of 8.72 days in the rest frame. We measured a time lag of $25.4^{+2.0}_{-1.4}$ days, which is much longer than the result reported in Denney et al. (2010). It is not unexpected because, with a similar spectroscopic aperture, the fluxes in our campaign ($\sim 3.9 \times 10^{-15}$ erg s^{-1} cm^{-2} Å^{-1}) are much higher than those ($\sim 0.9 \times 10^{-15}$ erg s^{-1} cm^{-2} Å^{-1}) in Denney et al. (2010). The BH mass obtained from our campaign is $2.89^{+0.25}_{-0.19} \times 10^7 M_\odot$ and is almost the same as that determined by Denney et al. (2010). Denney et al. (2010) did not resolve the lags at different velocities. In our campaign, the data also do not allow us to give high-quality velocity-resolved lag measurements. However, the general structure of velocity-resolved lags implies complicated BLR geometry or kinematics.

PG 1613+658 (Mrk 876): This object was monitored during 1991–1998 (Kaspi et al. 2000) and a Hβ time lag of $40.1^{+15.0}_{-15.2}$ was reported (Kaspi et al. 2005). The trough of the Hβ light curve is in the gap in Season 1, which gives a poorer constraint to the time lag than from Season 2. The Hβ time lag measured from Season 2 (with better data quality) is $48.3^{+5.0}_{-3.8}$ days, which is similar to the value in (Kaspi et al. 2005) but much better constrained. The profile of broad Hβ shows a strong red asymmetry and does not show significant changes compared to that of Boroson & Green (1992), Erkens et al. (1995), and Kaspi et al. (2000). However, the Hβ profile plotted by De Robertis (1985) shows a much stronger red wing and a slightly blueshifted peak. The radius of the innermost part of its dusty torus ($334.1^{+42.4}_{-37.0}$ days) was measured by infrared reverberation mapping (Minezaki et al. 2019) and is larger by a factor of $\sim$7 compared with the BLR size in the present paper. Similar to the average lag determination, the gap in Season 1 makes the velocity-resolved lag measurement somewhat unreliable. The velocity-resolved lags of Season 2 indicate that its BLR is dominated by inflow.

4.2. H β Asymmetry and BLR Kinematics

To investigate if there is any correlation between the Hβ asymmetry and BLR kinematics, we make a short summary in Table 8. Although the size of the present sample is limited, it is obvious that the kinematics of the Keplerian/virialized motion and inflow is more common than outflow, in particular in the objects with broader Hβ (e.g., FWHM (Hβ) $\gtrsim$ 4000 km s^{-1}, corresponding to Population B in Marziani et al. 2003b), similar to the cases reported in the literature (e.g., Bentz et al. 2009; Denney et al. 2010; Grier et al. 2013; Du et al. 2016a). It appears that the asymmetry of the emission line does not directly correlate with the BLR kinematics (e.g., red-asymmetric lines can be associated with inflow, outflow, or Keplerian/virialized BLR kinematics). This is consistent with the fact that the emission-line profile is the integration of the clouds in BLR and has relatively stronger degeneracy than the velocity-resolved lags for the BLR geometry and kinematics. The flux ratios of Fe II (from 4434 to 4684 Å) and Hβ lines ($R_{\rm Fe}$) are also listed in Table 8.

Parameter A listed in Table 1 is measured from an individual exposure with a high S/N ratio. We have checked that the variation in A is relatively weak (although not zero) for each object during the campaign. The "blue" or "red" asymmetry did not change in our observations. It is the same as expected because the varying part of the emission line is only a small portion of the entire profile. This can be justified from the much weaker emission lines in the rms spectra with respect to those in the mean spectra (see Figures 2–16). Therefore, it is enough to list parameter A measured from one individual exposure for exhibiting the blue or red asymmetry of the emission-line profiles for the present sample.

5. Summary

In this third paper of the series, we present the RM measurements of 15 PG targets from the MAHA project. Our campaign has both long-term duration (spans from 1 to 5 yr for different objects) and high cadence. We successfully measure reverberation time lags between the continuum and Hβ light curves for individual seasons using three different methods (ICCF, χ^2, and MICA). ICCF and MICA show more consistent results, while the χ^2 method demonstrates slightly larger scatter. The BH masses of PG 0049+171, PG 0923+129, PG 0947+396, PG 1001+054, PG 1048+342, PG 1100+772, PG 1202+281, PG 1310−108, PG 1351+640 are reported for the first time. The velocity-resolved lags of the objects are also measured and show very diverse kinematics (virialized, inflow, and outflow signatures). The results from the present sample suggest that the BLR kinematics of Keplerian/virialized motion and inflow is more common than that of outflow. Future BLR modeling will investigate their BLR geometry and kinematics in more detail.

We thank the anonymous referee for valuable comments that improved the article. We thank WIRO engineers James Weger, Conrad Vogel, and Andrew Hudson for their indispensable and invaluable assistance. We also acknowledge the valuable support from the staff of the Lijiang 2.4 m telescope, CAHA 2.2 m telescope, Asiago 1.82 m telescope, and SAAO 1.9 m telescope. Funding for the Lijiang 2.4 m telescope has been provided by CAS and the Peoples Government of Yunnan Province. This work is partly based on observations collected at the Centro Astronómico Hispanoen Andalucía (CAHA) at Calar Alto, operated jointly by the Andalusian Universities and the Instituto de Astrofísica de Andalucía (CSIC). This research is based in part on observations collected at Copernico telescope (Asiago, Italy) of the INAF—Osservatorio Astronomico di Padova. We thank the South African Astronomical Observatory for the allocation of telescope time, and Francois van Wyk for obtaining some of the spectra. We acknowledge the support by the National Science Foundation of China through grants NSFC-12022301, -11991051, -11991054, -11873048, -11833008, by National Key R&D Program of China (grants 2016YFA0400701), by grant No. QYZDJ-SSW-SLH007 from the Key Research Program of Frontier Sciences, Chinese Academy of Sciences (CAS), by the Strategic Priority Research Program of CAS grant No.XDB23010400, and by the International Partnership Program of CAS, grant No.113111 KYSB20200014. L.C.H. was supported by the National Science Foundation of China (11721303, 11991052) and the National Key R&D Program of China (2016YFA0400702). M.B. enjoyed support from the Chinese Academy of Sciences Presidents International Fellowship Initiative, grant No. 2018VMA0005. YRL acknowledges financial support from the National Natural Science Foundation of China through

grant NSFC-11922304 and from the Youth Innovation Promotion Association CAS. H.C. acknowledges financial support from grant NSFC-12122305. We also acknowledge support from a University of Wyoming Science Initiative Faculty Innovation Seed grant. This work is supported by the National Science Foundation under REU grant AST 1852289. T.E.Z. acknowledges support from NSF grant 1005444I.

This work is also based on observations obtained with the Samuel Oschin 48 inch Telescope at the Palomar Observatory as part of the Zwicky Transient Facility project. ZTF is supported by the National Science Foundation under grant No. AST-1440341 and a collaboration including Caltech, IPAC, the Weizmann Institute for Science, the Oskar Klein Center at Stockholm University, the University of Maryland, the University of Washington, Deutsches Elektronen-Synchrotron and Humboldt University, Los Alamos National Laboratories, the TANGO Consortium of Taiwan, the University of Wisconsin at Milwaukee, and Lawrence Berkeley National Laboratories. Operations are conducted by COO, IPAC, and UW. This work makes use of the public data from ASAS-SN project. ASAS-SN is supported by the Gordon and Betty Moore Foundation through grant GBMF5490 to the Ohio State University, and NSF grants AST-1515927 and AST-1908570. Development of ASAS-SN has been supported by NSF grant AST-0908816, the Mt. Cuba Astronomical Foundation, the Center for Cosmology and AstroParticle Physics at the Ohio State University, the Chinese Academy of Sciences South America Center for Astronomy (CAS- SACA), the Villum Foundation, and George Skestos.

Software: DASpec (https://github.com/PuDu-Astro/DASpec), PyCALI (Li et al. 2014), MICA (Li et al. 2016).

ORCID iDs

Dong-Wei Bao https://orcid.org/0000-0003-2024-1648
Michael S. Brotherton https://orcid.org/0000-0002-1207-0909
Pu Du https://orcid.org/0000-0002-5830-3544
Jacob N. McLane https://orcid.org/0000-0003-1081-2929
Bi-Xuan Zhao https://orcid.org/0000-0002-1007-1991
Sha-Sha Li https://orcid.org/0000-0003-3823-3419
Yu-Yang Songsheng https://orcid.org/0000-0003-4042-7191
Yan-Rong Li https://orcid.org/0000-0001-5841-9179
Bo-Wei Jiang https://orcid.org/0000-0003-3825-0710
David H. Kasper https://orcid.org/0000-0003-0534-6388
William T. Chick https://orcid.org/0000-0002-8818-6780
Jaya Maithil https://orcid.org/0000-0002-4423-4584
H. A. Kobulnicky https://orcid.org/0000-0002-4475-4176
D. A. Dale https://orcid.org/0000-0002-5782-9093
Hartmut Winkler https://orcid.org/0000-0003-2662-0526
Paola Marziani https://orcid.org/0000-0002-6058-4912
Mauro D'Onofrio https://orcid.org/0000-0001-6441-9044
Ming Xiao https://orcid.org/0000-0001-5981-6440
Bożena Czerny https://orcid.org/0000-0001-5848-4333
Jesús Aceituno https://orcid.org/0000-0003-0487-1105
Luis C. Ho https://orcid.org/0000-0001-6947-5846
Jian-Min Wang https://orcid.org/0000-0001-9449-9268

References

Barth, A. J., Bennert, V. N., Canalizo, G., et al. 2015, ApJS, 217, 26
Barth, A. J., Pancoast, A., Bennert, V. N., et al. 2013, ApJ, 769, 128
Begelman, M. C., Blandford, R. D., & Rees, M. J. 1980, Natur, 287, 307
Bentz, M. C., Denney, K. D., Grier, C. J., et al. 2013, ApJ, 767, 149
Bentz, M. C., Walsh, J. L., Barth, A. J., et al. 2008, ApJ, 689, L21
Bentz, M. C., Walsh, J. L., Barth, A. J., et al. 2009, ApJ, 705, 199
Blandford, R. D., & McKee, C. F. 1982, ApJ, 255, 419
Bon, E., Jovanović, P., Marziani, P., et al. 2012, ApJ, 759, 118
Boroson, T. A., & Green, R. F. 1992, ApJS, 80, 109
Boroson, T. A., Persson, S. E., & Oke, J. B. 1985, ApJ, 293, 120
Brewer, B. J., Partay, L. B., & Csanyi, G. 2011, Stat. Comput., 21, 649
Brotherton, M. S., Du, P., Xiao, M., et al. 2020, ApJ, 905, 77
Bruzual, G., & Charlot, S. 2003, MNRAS, 344, 1000
Capriotti, E., Foltz, C., & Byard, P. 1979, ApJ, 230, 681
Chen, K., & Halpern, J. P. 1989, ApJ, 344, 115
Chen, K., Halpern, J. P., & Filippenko, A. V. 1989, ApJ, 339, 742
Clavel, J., Reichert, G. A., Alloin, D., et al. 1991, ApJ, 366, 64
Czerny, B., Hryniewicz, K., Maity, I., et al. 2013, A&A, 556, A97
Czerny, B., Olejak, A., Rałowski, M., et al. 2019, ApJ, 880, 46
Dalla Bontà, E., Peterson, B. M., Bentz, M. C., et al. 2020, ApJ, 903, 112
Danehkar, A., Nowak, M. A., Lee, J. C., et al. 2017, ApJ, 853, 165
De Robertis, M. 1985, ApJ, 289, 67
De Rosa, G., Fausnaugh, M. M., Grier, C. J., et al. 2018, ApJ, 866, 133
Denney, K. D., Peterson, B. M., Pogge, R. W., et al. 2009, ApJL, 704, L80
Denney, K. D., Peterson, B. M., Pogge, R. W., et al. 2010, ApJ, 721, 715
Du, P., Brotherton, M. S., Wang, K., et al. 2018a, ApJ, 869, 142
Du, P., Hu, C., Lu, K.-X., et al. 2014, ApJ, 782, 45
Du, P., Hu, C., Lu, K.-X., et al. 2015, ApJ, 806, 22
Du, P., Lu, K.-X., Hu, C., et al. 2016a, ApJ, 820, 27
Du, P., Lu, K.-X., Zhang, Z.-X., et al. 2016b, ApJ, 825, 126
Du, P., & Wang, J.-M. 2019, ApJ, 886, 42
Du, P., Zhang, Z.-X., Wang, K., et al. 2018b, ApJ, 856, 6
Edelson, R., Turner, T. J., Pounds, K., et al. 2002, ApJ, 568, 610
Eracleous, M., Boroson, T. A., Halpern, J. P., & Liu, J. 2012, ApJS, 201, 23
Eracleous, M., Livio, M., Halpern, J. P., & Storchi-Bergmann, T. 1995, ApJ, 438, 610
Erkens, U., Wagner, S. J., Alloin, D., et al. 1995, A&A, 296, 90
Fausnaugh, M. M. 2017, PASP, 129, 024007
Fausnaugh, M. M., Grier, C. J., Bentz, M. C., et al. 2017, ApJ, 840, 97
Ferland, G. J., Netzer, H., & Shields, G. A. 1979, ApJ, 232, 382
Fu, H., & Stockton, A. 2009, ApJ, 690, 953
Gaskell, C. M., & Peterson, B. M. 1987, ApJS, 65, 1
Gaskell, C. M., & Sparke, L. S. 1986, ApJ, 305, 175
Gilbert, G. M., Riley, J. M., Hardcastle, M. J., et al. 2004, MNRAS, 351, 845
Grier, C. J., Pancoast, A., Barth, A. J., et al. 2017, ApJ, 849, 146
Grier, C. J., Peterson, B. M., Horne, K., et al. 2013, ApJ, 764, 47
Grier, C. J., Peterson, B. M., Pogge, R. W., et al. 2012, ApJ, 755, 60
Grier, C. J., Trump, J. R., Shen, Y., et al. 2017, ApJ, 851, 21
Ho, L. C., & Kim, M. 2014, ApJ, 789, 17
Horne, K., De Rosa, G., Peterson, B. M., et al. 2021, ApJ, 907, 76
Hu, C., Du, P., Lu, K. X., et al. 2015, ApJ, 804, 128
Hu, C., Li, S.-S., Guo, W.-J., et al. 2020a, ApJ, 905, 75
Hu, C., Li, Y. R., Du, P., et al. 2020b, ApJ, 890, 71
Hu, C., Wang, J.-M., Ho, L. C., et al. 2008, ApJ, 687, 78
Jackson, N., & Browne, I. W. A. 1989, MNRAS, 236, 97
Ji, X., Lu, Y., Ge, J., Yan, C., & Song, Z. 2021, ApJ, 910, 101
Kaspi, S., Brandt, W. N., Maoz, D., et al. 2017, FrASS, 4, 31
Kaspi, S., Brandt, W. N., Maoz, D., et al. 2021, ApJ, 915, 129
Kaspi, S., Maoz, D., Netzer, H., et al. 2005, ApJ, 629, 61
Kaspi, S., Smith, P. S., Netzer, H., et al. 2000, ApJ, 533, 631
Kochanek, C. S., Shappee, B. J., Stanek, K. Z., et al. 2017, PASP, 129, 104502
Kovačević, A. B., Wang, J.-M., & Popović, L. Č. 2020, A&A, 635, A1
Li, H. Z., Xie, G. Z., Dai, H., et al. 2010, NewA, 15, 254
Li, S.-S., Yang, S., Yang, Z.-X., et al. 2021, ApJ, 920, 9
Li, Y.-R., Songsheng, Y.-Y., Qiu, J., et al. 2018, ApJ, 869, 137
Li, Y.-R., Wang, J.-M., & Bai, J.-M. 2016, ApJ, 831, 206
Li, Y.-R., Wang, J.-M., Ho, L. C., et al. 2016, ApJ, 822, 4
Li, Y.-R., Wang, J.-M., Ho, L. C., Du, P., & Bai, J.-M. 2013, ApJ, 779, 110
Li, Y. R., Wang, J. M., Hu, C., Du, P., & Bai, J. M. 2014, ApJL, 786, L6
Lira, P., Kaspi, S., Netzer, H., et al. 2018, ApJ, 865, 56
Lu, K.-X., Du, P., Hu, C., et al. 2016, ApJ, 827, 118
Maoz, D., Netzer, H., Leibowitz, E., et al. 1990, ApJ, 351, 75
Marziani, P., Sulentic, J. W., Zamanov, R., et al. 2003a, ApJS, 145, 199
Marziani, P., Zamanov, R. K., Sulentic, J. W., & Calvani, M. 2003b, MNRAS, 345, 1133
Masci, F. J., Laher, R. R., Rusholme, B., et al. 2019, PASP, 131, 018003
Minezaki, T., Yoshii, Y., Kobayashi, Y., et al. 2019, ApJ, 886, 150
Netzer, H., & Trakhtenbrot, B. 2007, ApJ, 654, 754

Oknyansky, V. L., Brotherton, M. S., Tsygankov, S. S., et al. 2021, MNRAS, 505, 1029
Onken, C. A., Ferrarese, L., Merritt, D., et al. 2004, ApJ, 615, 645
Pancoast, A., Brewer, B. J., & Treu, T. 2011, ApJ, 730, 139
Pancoast, A., Brewer, B. J., Treu, T., et al. 2014, MNRAS, 445, 3073
Peterson, B., Wanders, I., Horne, K., et al. 1998, PASP, 110, 660
Peterson, B. M. 1993, PASP, 105, 247
Peterson, B. M., Berlind, P., Bertram, R., et al. 2002, ApJ, 581, 197
Peterson, B. M., Ferrarese, L., Gilbert, K. M., et al. 2004, ApJ, 613, 682
Planck Collaboration, Ade, P. A. R., Aghanim, N., et al. 2014, A&A, 571, A16
Planck Collaboration, Aghanim, N., Akrami, N., et al. 2020, A&A, 641, A6
Pounds, K. A., Reeves, J. N., King, A. R., et al. 2003, MNRAS, 345, 705
Press, W. H., Teukolsky, S. A., Vetterling, W. T., & Flannery, B. P. 1992, Numerical Recipes in FORTRAN. The Art of Scientific Computing
Rafter, S. E., Kaspi, S., Behar, E., Kollatschny, W., & Zetzl, M. 2011, ApJ, 741, 66
Rakshit, S., Woo, J. H., Gallo, E., et al. 2019, ApJ, 886, 93
Rodríguez-Pascual, P. M., Alloin, D., Clavel, J., et al. 1997, ApJS, 110, 9
Romero, G. E., Chajet, L., Abraham, Z., & Fan, J. H. 2000, A&A, 360, 57
Santos-Lleó, M., Clavel, J., Schulz, B., et al. 2001, A&A, 369, 57
Schlafly, E. F., & Finkbeiner, D. P. 2011, ApJ, 737, 103
Schmidt, M., & Green, R. F. 1983, ApJ, 269, 352
Shang, Z., Wills, B. J., Wills, D., & Brotherton, M. S. 2007, AJ, 134, 294
Shappee, B. J., Prieto, J. L., Grupe, D., et al. 2014, ApJ, 788, 48
Shen, Y., Horne, K., Grier, C. J., et al. 2016, ApJ, 818, 30
Shen, Y., & Loeb, A. 2010, ApJ, 725, 249
Songsheng, Y.-Y., Xiao, M., Wang, J.-M., & Ho, L. C. 2020, ApJS, 247, 3
Stockton, A., & Mackenty, J. W. 1983, Natur, 305, 678
Storchi-Bergmann, T., Nemmen da Silva, R., Eracleous, M., et al. 2003, ApJ, 598, 956
Sulentic, J. W. 1989, ApJ, 343, 54
Teräsranta, H., Wiren, S., Koivisto, P., Saarinen, V., & Hovatta, T. 2005, A&A, 440, 409
U, V., Barth, A. J., Vogler, H. A., et al. 2022, ApJ, 925, 52
van Groningen, E., & Wanders, I. 1992, PASP, 104, 700
Wang, J.-M., Du, P., Brotherton, M. S., et al. 2017, NatAs, 1, 775
Wang, J.-M., Songsheng, Y.-Y., Li, Y.-R., & Yu, Z. 2018, ApJ, 862, 171
Williams, P. R., Pancoast, A., Treu, T., et al. 2018, ApJ, 866, 75
Winkler, H., & Paul, B. 2017, arXiv:1708.02056
Woo, J.-H., Cho, H., Gallo, E., et al. 2019, NatAs, 3, 755
Woo, J.-H., Treu, T., Barth, A. J., et al. 2010, ApJ, 716, 269
Woo, J.-H., Yoon, Y., Park, S., Park, D., & Kim, S. C. 2015, ApJ, 801, 38
Xiao, M., Du, P., Horne, K., et al. 2018, ApJ, 864, 109
Yu, Z., Martini, P., Penton, A., et al. 2021, MNRAS, 507, 3771
Zajaček, M., Czerny, B., Martinez-Aldama, M. L., et al. 2020, ApJ, 896, 146
Zajaček, M., Czerny, B., Martinez-Aldama, M. L., et al. 2021, ApJ, 912, 10
Zakamska, N. L., Hamann, F., Pâris, I., et al. 2016, MNRAS, 459, 3144
Zhang, Z. X., Du, P., Smith, P. S., et al. 2018, ApJ, 876, 49